Journal of Magnetic Resonance 308 (2019) 106591

Contents lists available at ScienceDirect

Journal of Magnetic Resonance

journal homepage: www.elsevier.com/locate/jmr

An easily reproducible, hand-held, single-sided, MRI sensor

Mason Greer, Cheng Chen, Soumyajit Mandal *

Case Western Reserve University, 10900 Euclid Ave, Cleveland, OH 44106, USA

ARTICLE INFO

Article history:
Received 13 May 2019
Revised 29 August 2019
Accepted 3 September 2019
Available online 13 September 2019

Keywords:
Single-sided NMR
NMR-MOUSE
Portable MRI

ABSTRACT

Single-sided MRI sensors allow the imaging of samples that are larger than the magnet. Thus, they enable truly portable imagers with potential applications in medicine, quality assurance (QA), agriculture, material science, and other fields. However, despite recent advancements, single-sided MRI systems are relatively uncommon. This is partially due to the limited number of commercial products. Also, current implementations often require large and/or complex magnet arrays which require machining techniques such as milling or drilling. These techniques must be performed to tight tolerances to ensure accuracy of the B_0 field. Furthermore, these systems generally have hand-wound RF or gradient coils that are not trivial to construct. The main goals of this work are to reduce the size of single-sided MRI sensors while simultaneously making them more accessible for others to build. To this end, we present a hand-held, single-sided, MRI sensor that is constructed using an easy-to-assemble magnet array, a 3D-printed housing, and printed circuit boards (PCBs) that contain the RF coil, gradient coils, and matching network. By implementing all coils directly on PCBs, the geometry can be easily optimized and then manufactured at low cost. Both spin density-weighted and T_1-weighted images of various samples are presented to demonstrate the capabilities of the proposed sensor.

1. Introduction

Portable MRI systems using enclosed magnet geometries have been developed with good results [1], but are generally still too heavy to be transported easily. On the other hand, advances in single-sided NMR have led to the development of single-sided MRI sensors [2–4]. Such sensors allow for the imaging of a portion of any sample, regardless of its size, by placing the sample on the outside of the magnet as opposed to inside an enclosed geometry. The single-sided configuration enables truly portable NMR or MRI systems that can be utilized in many fields such as medicine, quality assurance (QA), agriculture, material science, and chemistry in situations where conventional MRI or NMR magnets are not practical [5–8]. However, despite the many potential applications, single-sided MRI systems are relatively underutilized. One potential reason for this is there are not many commercial options for single-sided NMR devices, let alone single-sided MRI devices. Without commercial options, one is forced to develop one's own device. However, most existing single-sided implementations are constructed of complex and/or bulky magnet arrays of considerable weight and require some level of machining to build. Furthermore, current implementations also utilize specialized hand-wound radio frequency (RF) and/or gradient coils that are not trivial to wind [4,9]. These challenges create a barrier for others to utilize single-sided MRI in their own work. In this paper, we aim to address these issues by constructing a hand-held MRI sensor out of a 3D-printed housing and printed circuit boards (PCBs) that contain the RF coil, gradient coils, and matching network.

A universal challenge for single-sided NMR and MRI sensors is low signal-to-noise ratio (SNR) due to large B_0 inhomogeneity and also poor coupling to the RF coil. Typical single-sided NMR/MRI sensors employ permanent magnets that project a B_0 field above the magnet array. The strength of this field falls off quickly with distance, leading to a large B_0 gradient. Collecting data in this grossly inhomogeneous region introduces several challenges. One of the main issues that arises is very thin slice thickness for RF pulses of a given bandwidth, which reduces the overall SNR. Thus, it is important to minimize the B_0 gradient in order to obtain sufficient SNR per scan.

The large static gradient also (i) limits imaging pulse sequences to be purely phase-encoded, and (ii) introduces large amounts of signal attenuation due to diffusion [10]. Overall SNR can be improved by using a Carr-Purcell-Meiboom-Gill (CPMG)-like pulse sequence to collect many spin echoes at every voxel in k-space. Spatial encoding is based on applying pulsed field gradients (PFGs) in between excitation and refocusing pulses of the CPMG sequence

* Corresponding author.
E-mail addresses: mkg53@case.edu (M. Greer), cxc717@case.edu (C. Chen), sxm833@case.edu (S. Mandal).

https://doi.org/10.1016/j.jmr.2019.106591
1090-7807/

[4]. Diffusion during this encoding period causes signal attenuation. This fact results in a trade-off between SNR and spatial resolution: the PFGs must be longer to obtain higher resolution, which increases signal attenuation. This issue is particularly important for low-viscosity liquids (e.g., water) due to their high diffusion coefficients. Thus, a smaller static gradient can significantly improve SNR for a given resolution.

Although the static gradient plays a large role in overall SNR, there are many other factors that contribute to low SNR in single-sided data acquisition. Such factors include relatively small detection area, low B_0 strengths, and poor B_1 coupling to the sample. Signal averaging improves total SNR but at the cost of longer acquisition times, which are undesirable from the user's point of view. Moreover, temperature drift of the magnets during long experiments can affect the B_0 distribution and thus generate image distortion. As a result, it is important to reduce total imaging time by maximizing SNR per scan.

To combat these issues, we develop a simple, truly portable magnet that is small enough to fit in the palm of the hand. The magnet is specifically designed to minimize the intrinsic B_0 gradient while keeping the field uniform over the slice of interest. A smaller static gradient also increases the slice thickness, i.e., the total sample volume. In order to reduce manufacturing complexity, the sensor housing is 3D printed and all other components (RF coil, gradients, and matching network) are manufactured on PCBs. Moreover, all relevant design files have been uploaded to a public repository[1] to enable others to easily reproduce the design. The magnet itself is constructed from low-cost parts (five standard neodymium (NdFeB) magnets and three copper shields) that can be purchased from a variety of vendors. In this paper, we will discuss the design of this sensor and show preliminary experimental results.

2. Methods

2.1. Sensor overview

The sensor is comprised of a magnet harness, five NdFeB magnets, three copper shields, and PCBs containing the RF coil, RF shield, gradient coils, and matching network as shown in Fig. 1. The magnet harness is 3D printed from a common thermoplastic polymer, namely acrylonitrile butadiene styrene (ABS), to ensure easy prototyping and reproducibility. It is important that the material used is a stronger plastic such as ABS or polycarbonate. Weaker 3D-printed materials such as polylactic acid (PLA) are not structurally sound enough to hold the magnets in place without breaking. To achieve the highest field strength possible, the magnets used in this design were all N52-grade NdFeB pieces purchased from K&J Magnetics. The sizes chosen in this work are all standard sizes and can be also be purchased easily from other vendors.

As with all permanent magnets, there is a variation in field strength from magnet to magnet as well as along the axis of each magnet. K&J Magnetics quotes a residual flux density of 1.45–1.48 T for their N52 NdFeB magnets. Despite this range, we do not attempt to carefully shim our field, instead operating in relatively non-uniform fields in order to keep the sensor simple to build. However, we do implement first-order shimming by placing set screws along each side of the magnets to hold them in a given location. The actual positions of the magnets can then be adjusted via the screws.

All of the circuitry and coils are manufactured on PCBs. In most existing single-sided MRI devices, coils are wound from magnet wire. Winding coils is time consuming, reproducibility is difficult, and complex geometries are challenging to realize [11]. By etching all the coils onto PCBs, the device can be easily designed and optimized through simulation and computer-aided design (CAD) software. The optimized designs can then be readily manufactured to well-defined tolerances provided by the PCB vendor. This helps explain why many commercial MRI systems use coils etched on rigid or flexible PCBS [12].

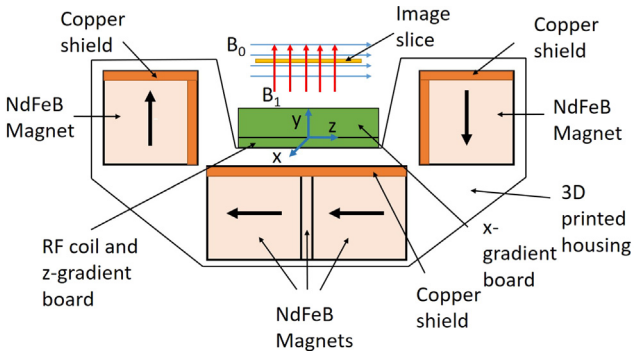

Fig. 1. A cross-sectional view of the proposed hand-held MRI sensor.

An important issue that affects single-sided devices is mechanical forces on the magnets due to eddy currents induced by strong RF fields [13,14]. Such forces result in vibrations of the magnet and coil that (i) distort the B_0 field, and (ii) increase the ringdown or "dead" time of the RF coil after each pulse (often to hundreds of μs) [13,14]. To reduce these vibrations, a thin copper shield is placed above the permanent magnets. The goal is for the eddy currents from the RF coil to circulate within the shield and not the magnets, thus reducing vibrations. The shield does reduce coil *Q*, which affects SNR. However, in our case the benefits of reduced dead time outweigh the cost of somewhat lower coil *Q*. Unwanted electromechanical vibrations are further reduced by proper mechanical design, in particular by ensuring that the entire sensor behaves as a single rigid object. Fortunately, PCB-based coils are naturally rigid, unlike hand-wound ones. If needed, vibrations can be further damped by adding mechanically-compliant material (e.g., epoxy) between the rigid components.

2.2. Magnet design

Optimizing the magnet design is essential in any MRI system. A strong gradient G_0 in the depth direction (i.e., pointing into the sample) is generated by all single-sided magnet configurations, which in turn defines an RF power-limited slice thickness in this direction. While the static gradient is useful for collecting diffusion-weighted data on viscous fluids, it unnecessarily reduces SNR when collecting non-diffusion-weighted data [15]. To address this issue, we develop a novel magnet array which minimizes the overall gradient while maintaining acceptable B_0 homogeneity and penetration depth. Typical single-sided sensors (e.g., the well-known NMR-MOUSE) have a flat upper surface, with the sample placed above it [2]. In this design, we use a curved geometry that results in higher B_0 by allowing the sample of interest to be partially enclosed by the magnet.

To optimize the magnet geometry, simulations were preformed using Radia, a free 3D magnetic field simulator based on the boundary integral method [16]. As shown in Fig. 1, we use two magnets with opposite polarization along the outside of the geometry and a third magnet below these two to focus the flux lines. To optimize the field, we sweep the positions of the top magnets along the *y* and *z* directions and consider two main parameters while optimizing the field, namely (i) SNR for a given RF power level, and (ii) field uniformity at a given depth.

[1] The design files are available here: https://github.com/Greerm2/Hand-Held-MRI.

As described by [17,18], SNR per unit volume increases as $B_0^{7/4}$ when thermal noise from the coil (assuming a skin effect-limited resistance) is the dominant noise source. A passive RF shield is placed above the coil to ensure that lossy samples are sufficiently decoupled from the coil, which will be described in more detail later. Thus, the SNR of the device should scale with $B_0^{7/4}$. It should also scale with sample volume, thus

$$SNR \propto B_0^{7/4} V_s, \tag{1}$$

where V_s is the volume of sample excited. The latter is directly proportional to slice thickness, which is inversely proportional to the static gradient. Thus, we can rewrite Eq. (1) as

$$SNR \propto \frac{{B_0}^{7/4}}{G_0}, \tag{2}$$

where G_0 is the static gradient. We also want B_0 to be as uniform as possible in the lateral plane, i.e., across the field of view (FOV) defined by the RF coil. In order to define a figure of merit for optimizing SNR and field uniformity, we divide Eq. (2) by the estimated root mean squared error (RMSE) of the field. The RMSE is calculated by

$$RMSE = \frac{\sqrt{\sum_i^N \left(\overline{B_0} - B_{0i}\right)^2}}{N}, \tag{3}$$

where $\overline{B_0}$ is the average B_0 field in the FOV, B_{0i} is the field at the i-th spatial point, and N is the total number of spatial points in the simulation. Utilizing the RMSE value, we define the figure of merit (FOM) to be

$$FOM = \left(\frac{{B_0}^{7/4}}{RMSE \times G_0}\right). \tag{4}$$

We then find the maximum value of Eq. (4), defined as $Opt = \max(FOM)$, which defines the optimum geometry under these constraints. In particular, this geometry provides the best-possible combination of SNR and field uniformity while utilizing the method described above. It should be noted that this is not the only possible metric for optimizing the geometry; however, it is a convenient one that provides good results in practice.

To start optimizing the geometry, we first pick suitable magnets for our given size constraint. In our case, we would like the entire sensor to fit in the palm of the hand. To keep the design within this limit, we use five small NdFeB magnets; four of these are $50.8 \times 12.7 \times 12.7$ mm in size, while the fifth has dimensions of $50.8 \times 12.7 \times 3.175$ mm. We chose magnets that are 50.8 mm long because this length should fit comfortably in the average person's hand. The width and height of the magnets were selected to be 12.7 mm, which is also small enough to ensure that the sensor will comfortably fit in the palm of the hand after assembly. A fifth magnet with a width of 3.175 mm was added in between the two bottom magnets to increase the width of the sensor and its FOV.

Based on this configuration of magnets, we then maximize Eq. (4) by varying the positions of these magnets subject to the overall size constraint. We start by defining the acceptable range of slice depths (with respect to the surface of RF coil PCB) to be 3–7 mm. Next, we conduct a 2D sweep of the magnet positions and record the B_0 value at each discrete location. For this procedure, we keep the bottom magnets stationary and sweep the separation of the top magnets along the z-direction as well as sweep their position along the y-direction. Fig. 2 illustrates the definitions for the simulation described above.

We start the simulation with the z-separation being 45 mm apart, as this is the closest we can keep the magnets while maintaining structural stability of the 3D printed housing. This is because we need 3D printed material to separate the top and bottom magnets from each other. If the thickness of the printed layer is too small, the magnetic forces can cause the housing to crack or completely break. The starting position of the top magnets along the y-direction is initially set to be 0, and is then increased in the positive y-direction up to a final separation of 10 mm.

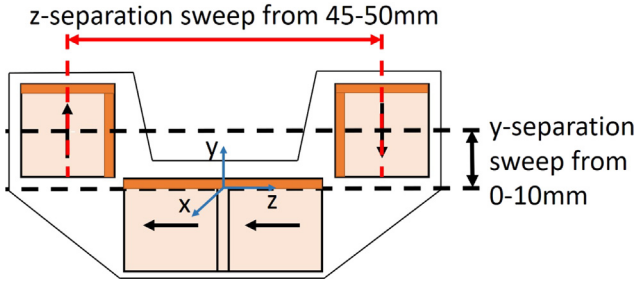

Fig. 2. The directions along which the magnets were swept when optimizing the sensor geometry.

The results of the optimization are shown in Fig. 3. Clearly, the optimal configurations are confined to a well-defined curve in the 2D optimization space. Different configurations of the magnets can be chosen along this curve while considering trade-offs between B_0 strength, B_0 uniformity, and G_0 strength. In this design, where small size is an important goal, we choose a z-separation of 45.7 mm in order to keep the design as compact as possible while ensuring structural integrity of the sensor. Based on this selection of z-separation, we find the optimal y-separation to be 5.4 mm. The optimal region seen on the plot is approximately a 0.4 mm × 0.4 mm box, which is within the manufacturing tolerance (0.12 mm) of the Fortus 400mc (Stratasys, Rehovot, Israel) 3D printer used to print the housing. It should be noted that the variations in field strength from magnet to magnet can make the chosen configuration less optimal. In order to keep the design simple, we do not analyze this issue further.

Fig. 4a shows the simulated B_0 field at various depths ranging from 4 to 8 mm. The slices are the most uniform in the middle of the intended FOV and then become non-uniform towards the edges. This can be seen more clearly in Fig. 4b, where the center

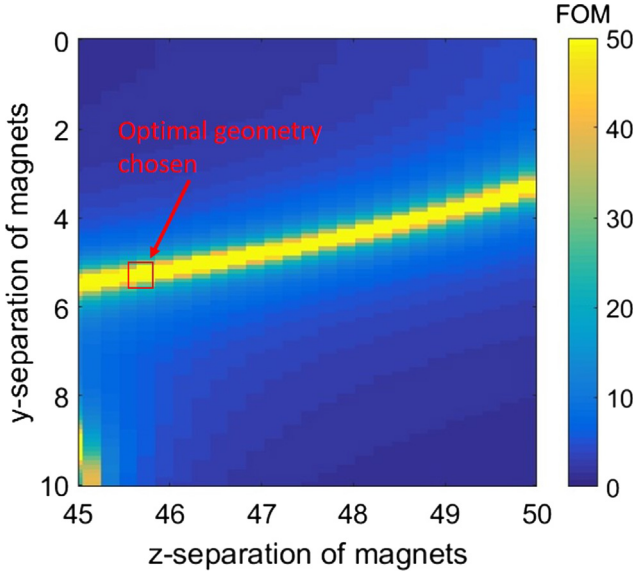

Fig. 3. Simulated figure of merit (SNR/(G_0× RMSE)) as a function of the y-separation and z-separation of the magnets. Separations of 45.7 mm (z-axis) and 5.4 mm (y-axis) are chosen as the optimal point. This point was chosen to keep the sensor compact. If size is not a major constraint, other points along the optimal curve can be chosen.

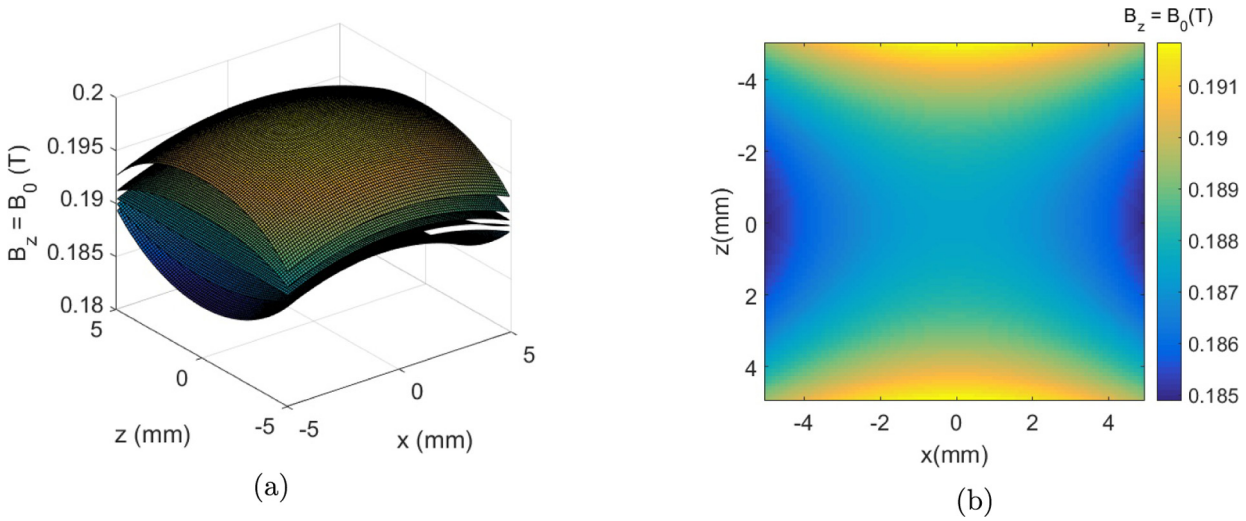

Fig. 4. (a) Simulated B_0 field slices at the chosen optimal configuration of the sensor. The slice depths (referred to the RF coil) from bottom to top are 7, 6, 5, 4, and 3 mm. (b) Plot of the field at a depth of 6 mm.

region is the most uniform and the field either increases or falls off at the edges. Such non-uniformities will cause distortions in the images due to parts of the sample being excited and detected at slightly different depths.

2.3. PCB design overview

As discussed above, the RF coil, RF shield, matching network, and gradient coils are all designed on PCBs. This allows for easy reproducibility and manufacturing of complex designs, and also minimizes the pulse ringdown by preventing the wires from vibrating. The system contains three separate boards of which two contain solenoidal *x*-gradients and the third contains the RF coil, matching network, and *z*-gradients. A cross-sectional view of the PCBs used in this design can be seen in Fig. 6a. It should be noted that this diagram is not drawn to scale; the RF and *z*-gradient PCB has been enlarged to show all six layers of the board in detail. The actual dimensions are summarized in Table 1. Top views of the solenoid board and RF board can be seen in Fig. 6c. The gradient design will be discussed in more detail in the sections below.

Table 1
Dimensions for Fig. 6a.

Parameter	Value
a	0.8 mm
b	3.175 mm
c	0.16 mm
d	15.4 mm
e	0.61 mm
f	13.1 mm
g	14.1 mm

The RF coil uses a planar spiral design (3 turns, inner diameter = 9 mm). Given the size constraint of the sensor, we set the outer diameter of the coil to be 13.1 mm, which leaves room for the planar gradients to be placed outside it. The FOV of the sensor is approximately equal to the inner diameter of the coil. Fig. 5a shows the simulated sensitivity profile of the RF coil at depths ranging from 4 to 8 mm, while Fig. 5b shows the profile of the B_1 field at a depth of 5 mm. Because of the relatively small coil, the sensitivity

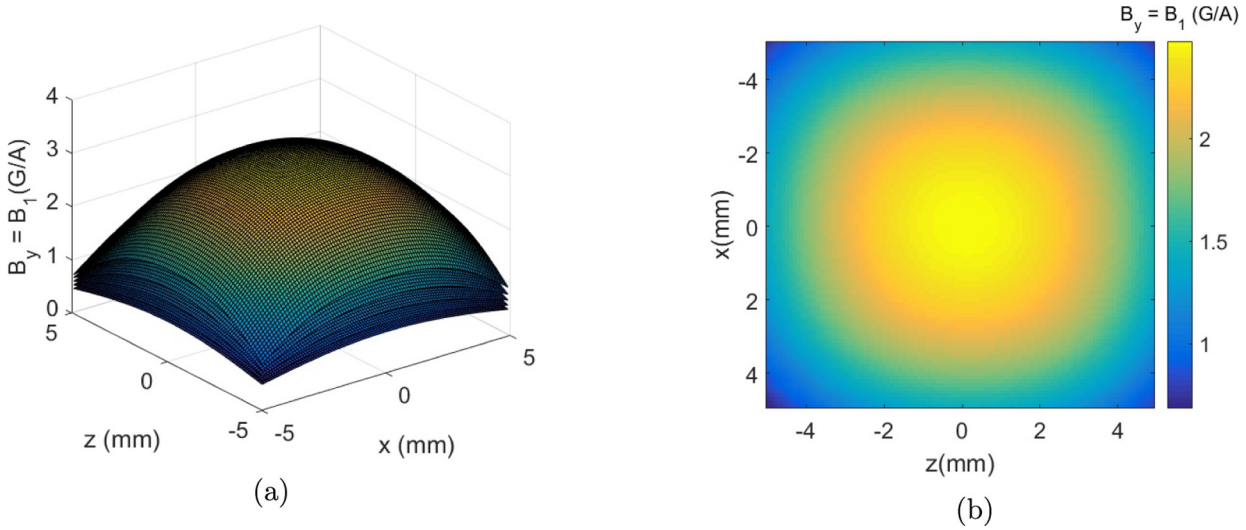

Fig. 5. (a) Simulated B_1 field in terms of Gauss per amp (G/A). The slices shown are at depths (from bottom to top) of 8, 7, 6, 5, and 4 mm. (b) Similar to the B_0 field, the B_1 sensitivity map decreases near the edges of the intended FOV, which will further distort the acquired images.

pattern is not completely uniform over the entire 9 × 9 mm target FOV. For example, at a depth of 6 mm, the field falls off from about 0.45 G/A (at the center) to 0.32 G/A (at the edges). As a result, the excitation and refocusing pulses will be relatively non-uniform across the sample. However, we show later that image distortion due to the non-uniform field can be corrected for if the sensitivity map is known.

Because the sensor is intended to be portable, it is important that it can operate in noisy environments. Noise can come from many sources including the internal circuitry and the external environment. Furthermore, a large sample can act as an antenna which amplifies and directly injects the external noise into the RF coil. To reduce such effects, a slotted shield is placed over top of the RF coil to terminate electric field lines before they reach the coil. The shield is slotted in order to reduce eddy currents during RF pulses. Although such a shield reduces the sensitivity and penetration depth of the coil, in practice the reduction in external interference more than compensates for this penalty [14]. We quantify this reduction experimentally in later sections.

Fig. 6b shows the schematic for the matching network used in this design. We use the common "L"-type two-capacitor network, which uses a parallel capacitor (C_p) and a series capacitor (C_s). C_p and C_s are both parallel combinations of (i) two fixed ceramic capacitors, and (ii) a variable (trimmer) capacitor. The values of the fixed capacitors are selected based on measured coil properties, while the trimmer capacitors are used to fine-tune the matching frequency.

2.4. Planar z-gradient design

The initial design of the z-gradient coils was based on that in [4], which used two planar coils wound in opposite directions. However, this configuration was not ideal for our small sensor. In particular, fitting all the coils in the small space between the two magnets resulted in simulations that showed relatively small and non-linear gradients across the sample.

Instead, we used a planar gradient coil geometry that consists of two wires running anti-parallel to each other. This design is both simpler to implement and uses a smaller total wire length, which also reduces the DC resistance R_{dc}. Lower values of R_{dc} are critical in portable applications since this minimizes the power consumption I^2R_{dc} required to generate a certain gradient strength.

To optimize the planar gradient coil, we used Radia to simulate the average and RMSE of the field gradient G_z over the targeted FOV as the locations of the wires vary from the outside of the RF coil to the edge of the PCB. Similar to Eq. (4), we used the average and RMSE values to define the following figure of merit for the gradient coil:

$$FOM = \frac{\overline{G}}{RMSE}, \tag{5}$$

where $\overline{G}$ is the average gradient strength across the FOV. The maximum value of this equation is the optimal separation of the gradient wires. In order to reduce coupling between the RF coil and the

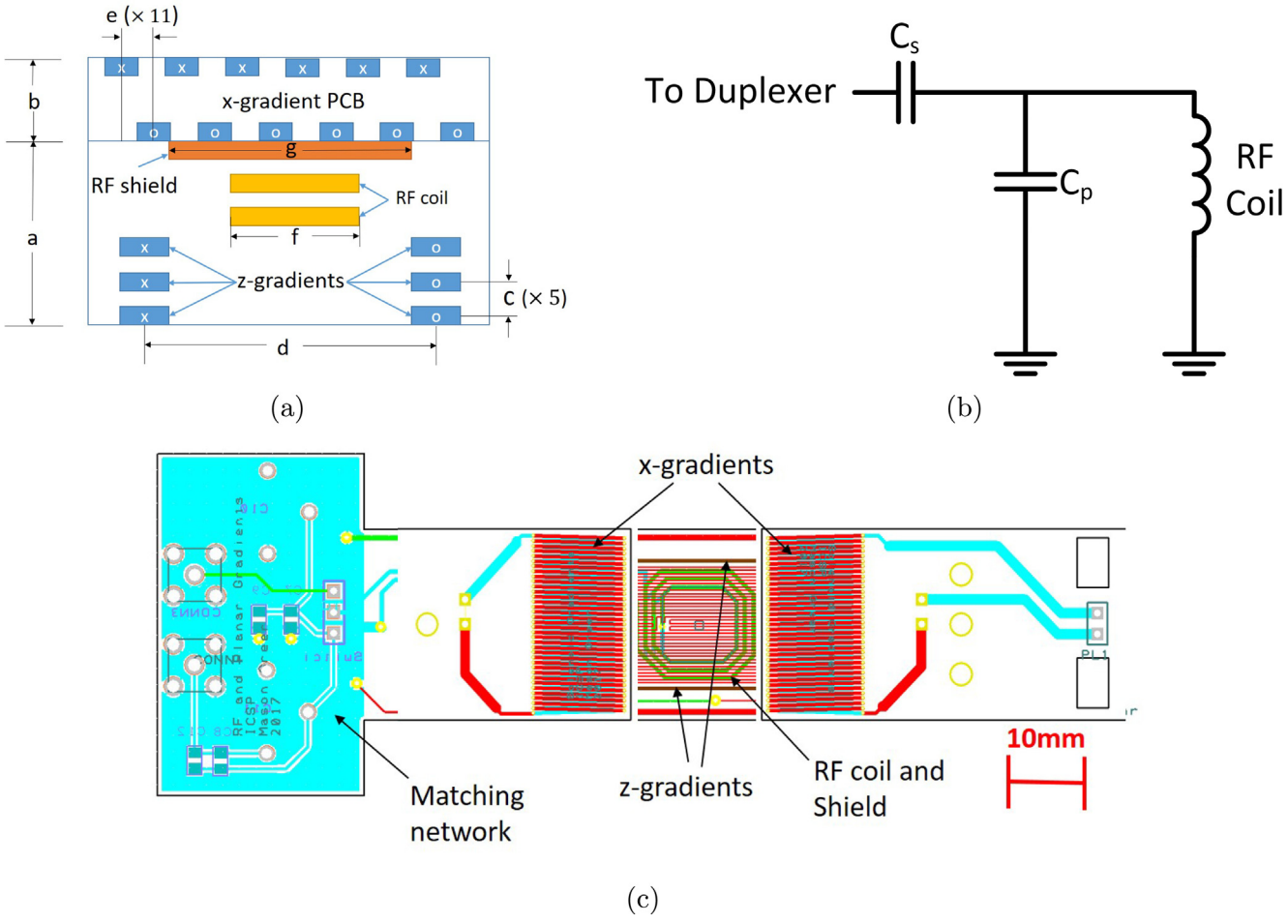

Fig. 6. (a) Cross-section of the PCBs containing the RF coil, RF shield, and gradients. For clarity, the diagram is not drawn to scale: the x-gradient PCB is significantly larger than the z-gradient and RF coil board, as indicated by the dimension labels. The actual dimensions are summarized in Table 1. (b) Schematic of matching network utilized in this design. (c) Top view of the PCBs designed for this sensor. The image shows the matching network, RF coil and shield, z-gradients and x-gradients.

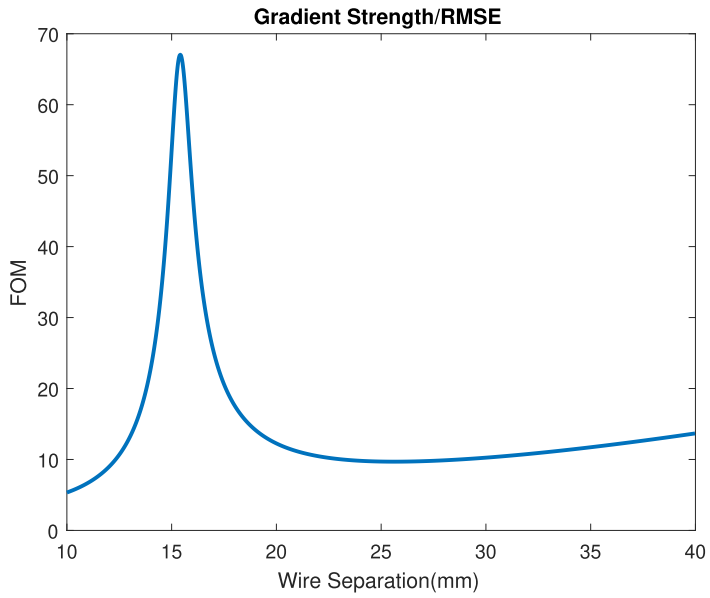

Fig. 7. Simulated figure of merit (Average/RMSE) of the z-gradient G_z as a function of separation between the coplanar wires in the gradient coil.

gradient, we do not consider placing the gradient wires under the RF coil. Fig. 7 plots the metric in Eq. (5) as a function of wire separation. The optimal separation for the given FOV is 15.4 mm. A top view of the z-gradient coil can be seen in Fig. 9c.

2.5. Solenoid x-gradient design

The design of the x-gradient coil is based on that described in [4]. In [4], two solenoids were wound in opposite directions and placed on opposite sides of the RF coil to generate the x-gradient G_x. However, instead of winding coils, we choose to implement them on PCBs, which introduces its own set of challenges. One particular challenge is creating a 3D geometry on a roughly 2D planar layout of PCB layers. In order to create a three-dimensional solenoid-like geometry with such layers, we use wires on both the top and bottom layers and connect them with plated through-hole vias as shown in Fig. 6. The vias act as short wires that connect the top and bottom layers of the board.

To maximize the gradient strength, we maximize the turn density of each solenoid. This was achieved by setting the via size and via-via spacing (i.e., pitch) to the smallest values allowed by the PCB manufacturer. For example, we used vias with an inner and outer diameter of 0.254 mm and 0.508 mm, respectively, and a pitch of 0.61 mm. To minimize R_{dc}, the wire width (0.45 mm) was then selected as the widest that is compatible with the design rules (via pitch and wire-wire spacing). Finally, the length of each solenoid was maximized (set to the width of the PCB) in order to improve gradient uniformity, i.e., reduce RMSE.

With the basic solenoid layouts completed, we simulated G_x as a function of the board thickness h. For this purpose, the solenoids were placed at their minimum separation, which is the diameter of the RF coil. Boards up to $h = 6.35$ mm thick were available from the manufacturer, but we set an upper limit of $h_{max} = 3.175$ mm since thick boards prevent large samples from being placed on the coil. Thus, the goal is to keep the boards as thin as possible while also providing sufficient gradient strength. Fig. 8a shows

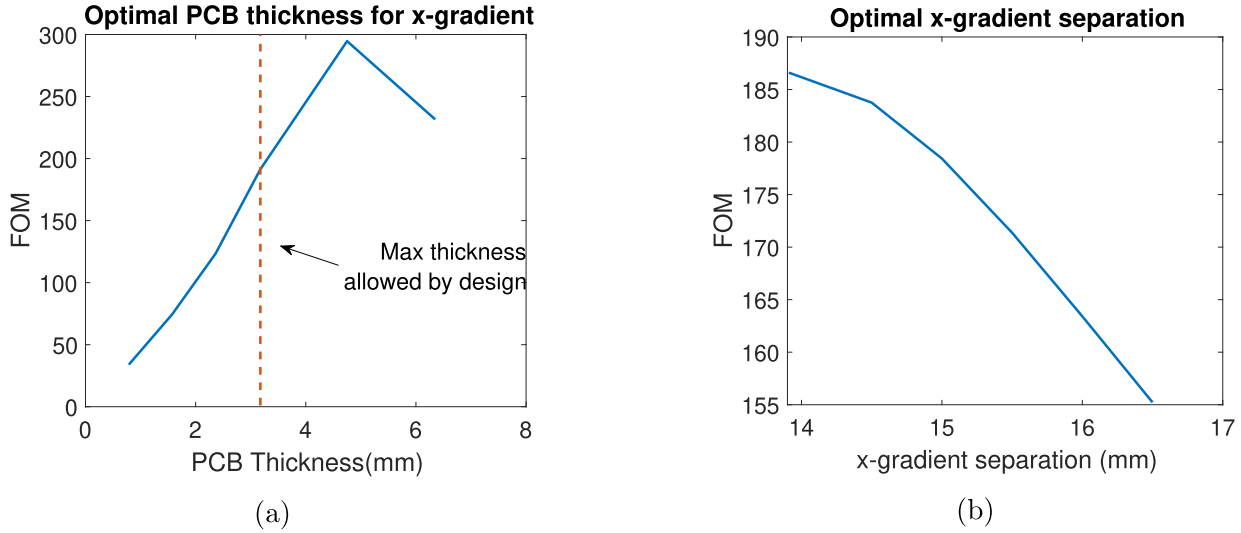

Fig. 8. (a) Simulated figure of merit (Average/RMSE) of the x-gradient G_x as a function of board thickness h. There is an optimum at $h_{opt} \approx 5$ mm, but we limit h to $h_{max} = 3.175$ mm as described in the text. (b) Simulated figure of merit for $h = h_{max}$ as a function of solenoid separation.

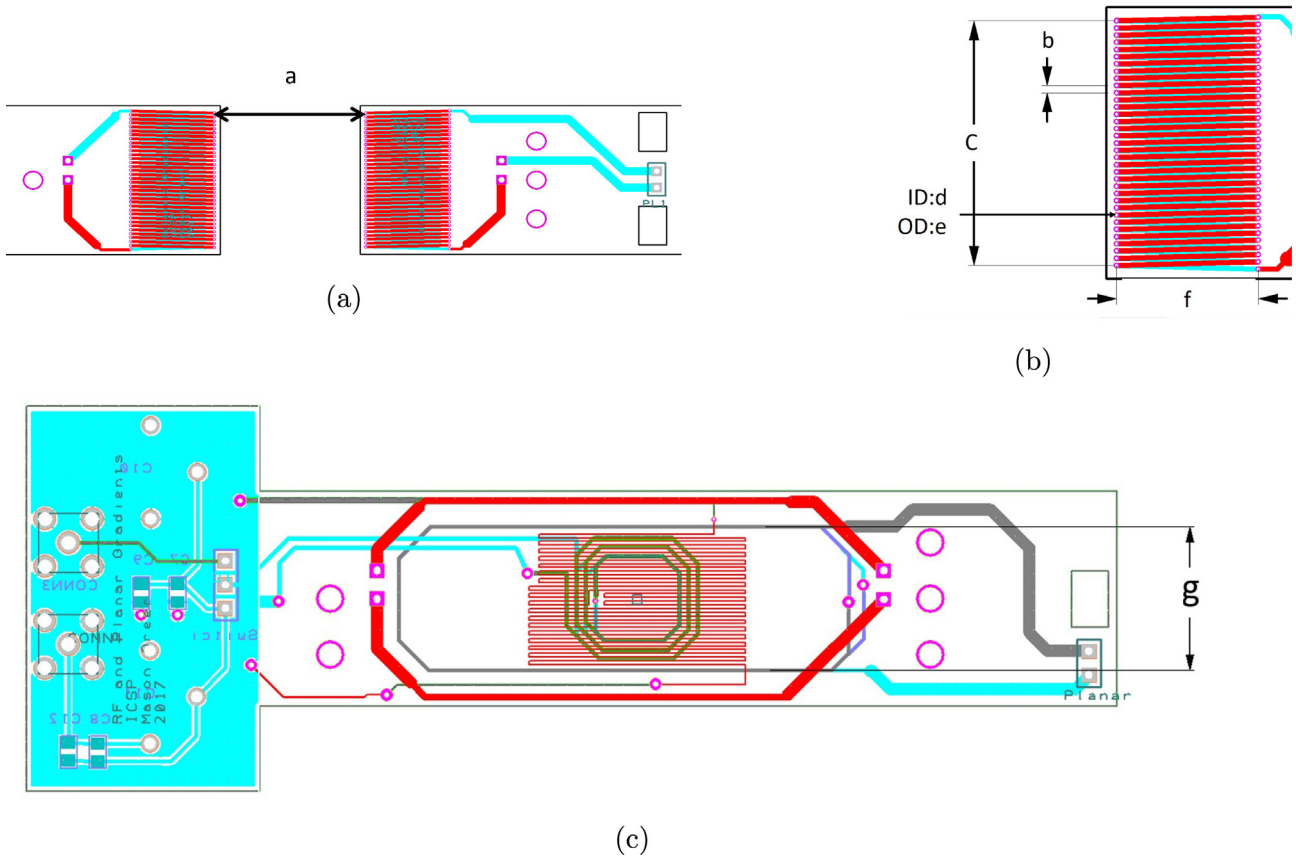

Fig. 9. (a)–(b) Design of the *x*-gradient coil: (a) separation between the two solenoids, and (b) dimensions of each solenoid. (c) Top view of the RF coil and *z*-gradient coil board. The separation between wires in the *z*-gradient coil is indicated. The actual dimensions are summarized in Table 2.

Table 2
Dimensions for Fig. 9.

Parameter	Value
a	13.91 mm
b	0.61 mm
c	20.73 mm
d	0.254 mm
e	0.508 mm
f	12 mm
g	15.4 mm

the (average gradient strength divided by the RMSE) as a function of h. The figure shows that the optimal thickness is $h_{opt} \approx 5$ mm. However, since $h_{opt} > h_{max}$, we are forced to use the slightly non-optimal value of $h = h_{max} = 3.175$ mm. Finally, the figure of merit was simulated as a function of separation between the solenoids. The results, which are summarized in Fig. 8b, show that the solenoids should be as close together as possible. Thus, we place them directly outside of the RF coil.

The width of each solenoid was chosen to be 12 mm since this was the maximum width that resulted in $R_{dc} < 1\ \Omega$. [2] Specifically, the final design had resistances of 0.91 Ω, 0.02 Ω, and 0.05 Ω for the solenoid wires, the vias, and the connecting wires, respectively, resulting in a total $R_{dc} = 0.98\ \Omega$. Fig. 9a shows the overall gradient coil design (including both solenoids), while Fig. 9b shows a zoomed-in version (including the dimensions described above). The actual dimensions for both these figures are summarized in Table 2.

2.6. Pulse sequence design

Data for 2D imaging is acquired using a CPMG-like pulse sequence as described in [4]. As shown in Fig. 10, the sequence contains an initial phase-encoding period followed by a CPMG-like series of refocusing pulses. The gradients are turned on during the encoding period. As a result, the initial echo time τ_1 is limited by the length of the longest gradient pulse. By default, all the spin echoes generated by the refocusing pulses are added to improve SNR. Thus, SNR can be maximized by using the minimum echo spacing $t_{E,min}$ allowed by the hardware.

In addition to the usual two- or four-part CPMG phase cycle, the imaging experiment must be done in two parts with the phases of the refocusing pulses varying by $\pi/2$ between the parts. In particular, we use *y*-pulses for part 1, and *x*-pulses for part 2 as shown in Fig. 10. This is because the in highly inhomogeneous B_0 fields, the asymptotic CPMG-like component of the magnetization is locked to the rotation axis defined by the refocusing cycle [19]. By contrast, magnetization that is perpendicular to this axis exhibits Carr-Purcell (CP)-like behavior and rapidly decays to zero after a few echoes. Because the applied phase encoding gradients spread the spins along the transverse direction into *x* and *y* components,

[2] This value was chosen to be compatible with a custom-designed miniature gradient driver circuit with voltage and current compliances of ±5 V and ±5 A, respectively. However, for convenience, benchtop power amplifiers (AE Techron 7224, Elkhart, IN) were used to drive the gradients in this work. Thus, we do not describe the miniaturized gradient driver.

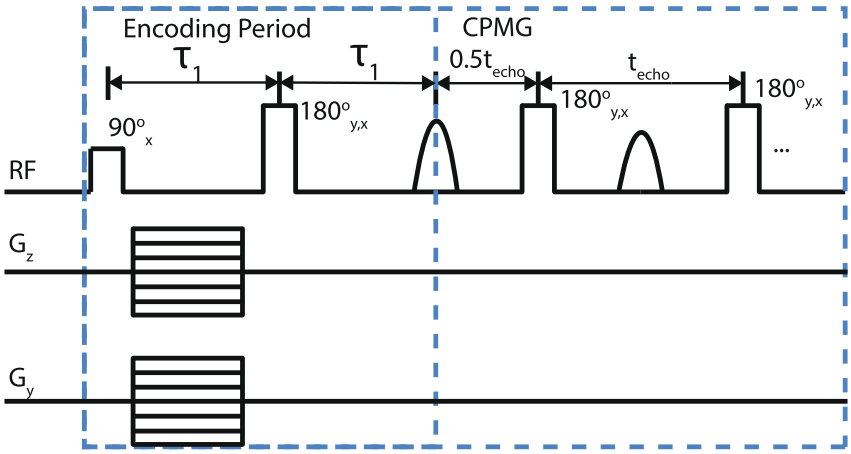

Fig. 10. The 2D imaging pulse sequence, which relies on pure phase encoding [14]. Each scan consists of (i) an encoding time, during which pulsed gradients provide spatial encoding; and (ii) a CPMG-like series of refocusing pulses, which generates a large number of spin echoes that are added to improve SNR. The sequence is applied in two parts, with the phases of the refocusing pulses changing by $\pi/2$ (x to y, or vice versa).

only half of the signal can be recovered. As a result, the reconstructed image suffers from aliasing. In order to eliminate such aliasing, the experiment is run twice with a $\pi/2$ phase shift between the refocusing axes. A complex-valued data set is then created by combining the real component of data acquired from part 1 with the imaginary component acquired from part 2, as follows:

$$s(m,n) = \mathrm{Re}\big(s_y(m,n)\big) + i\ \mathrm{Im}(s_x(m,n)), \tag{6}$$

where $s_y(m,n)$ and $s_x(m,n)$ are the signals recorded at voxel (m,n) during the y-and x-experiments, respectively. Images reconstructed from $s(m,n)$ do not suffer from aliasing, as expected, but at the cost of a $2\times$ increase in overall imaging time.

Adding up a series of spin echoes results in images with T_2 contrast, as described in earlier work on single-sided MRI sensors [4]. However, other contrast mechanisms are also possible. To describe these mechanisms, we start by writing the measured signal as

$$s(T_1,D,T_2) = \sum_{j=1}^{N_C} A_i e^{-2/3\gamma^2 G_0^2 D_j \tau_1^3}\Big(1-e^{-\left(t_W/T_{1j}\right)}\Big)\sum_{k=1}^{N_E} e^{-kt_E/T_{2j}}, \tag{7}$$

where N_E is the number of echoes, N_C is the number of unique components (e.g., regions) in the sample, A_i is the initial amplitude of each component, t_W is the wait time between scans, T_{1j} is the longitudinal relaxation time of each component, γ is the gyromagnetic ratio, G_0 is the static gradient, D_j is the diffusion coefficient of each component, τ_1 is the duration of the encoding period, and T_{2j} is the transverse relaxation time of each component. It is clear from Eq. (7) that the image contrast will in general be a function of signal amplitude, T_1, T_2, and D for each component in the sample.

It is possible to enhance T_2 contrast by dividing the echoes from a single scan into two groups (initial and later echoes), summing them separately to get two signals s_1 and s_2, and then finding the difference between them [4]. However, this process degrades SNR since the noise present in s_1 and s_2 is generally uncorrelated, and thus adds when we compute $s_1 - s_2$. It is also possible to enhance diffusion contrast by strategically choosing the encoding period τ_1. However, the images shown in this paper use the minimum possible value of τ_1 in order to maximize SNR.

In order to obtain enhanced T_1 contrast between two samples, we keep t_W approximately equal to the T_1 of one sample but much shorter than that of the other sample. Mathematically, we can show this by simplifying the problem to a sample with only two components. The signal then becomes

$$s(T_1,D,T_2) = A_1 e^{-2/3\gamma^2 G_0^2 D_1 \tau_1^3}\big(1-e^{-t_W/T_{1,1}}\big)\sum_{k=1}^{N_E} e^{-kt_E/T_{2,1}} + A_2 e^{-2/3\gamma^2 G_0^2 D_2 \tau_1^3}\big(1-e^{-t_W/T_{1,2}}\big)\sum_{k=1}^{N_E} e^{-kt_E/T_{2,2}}, \tag{8}$$

where $T_{1,1} < T_{1,2}$. If we choose t_W such that $T_{1,1} < t_W < T_{1,2}$, we will get a relatively large value of $t_W/T_{1,1}$, which decreases the exponential term and leaves the initial amplitude of component 1 relatively unaffected. The opposite will happen for component 2, which will be suppressed in the image since $t_W/T_{1,1}$ is relatively small. Moreover, the amount of T_2-weighting in the echo sums can be minimized by reducing N_E (i.e., the number of echoes) such that $N_E t_E < T_{2j}$ for $j = 1$ and 2. In this case, a significant amount of T_1 contrast will be generated.

3. Sensor characterization

3.1. Sensor construction

Fig. 11 shows a completely-assembled hand-held sensor including the magnet, shields, and all PCBS. The magnets are held in place using plastic set-screws that allow for the magnets to be moved or replaced if necessary. We measured the B_0 field with a F.W. Bell (Portland, OR) 5180 Gaussmeter and a F.W. Bell STD18-0404 transverse probe. The probe was mounted to a computer numerical control (CNC) machine and swept across the FOV. Fig. 12a shows the measured B_0 at a depth of 6 mm. When compared with the simulated field shown in Fig. 4b, the measured field has a slightly lower magnitude but a similar field profile to the simulated data. Also, the measured B_0 is more uniform along the x-direction than the simulated field profile, which will be discussed more later.

From Fig. 4b, it can be seen that there are two distinct regions of relatively uniform B_0 at ≈ 0.185 T and ≈ 0.186 T. This suggests that the image will be collected at slightly different depths across the FOV. In this specific case, the spins along the center of the z-axis will be excited at a slightly shallower depth the spins at the edges, which have a smaller B_0. The resulting images should have a bright area along the center of the z-axis and darker areas along the edges. The non-uniform B_1 field will tend to cause further distortion in the images. There is also a significant drop off in field strength around $x = -5$ mm suggesting significant distortion near this region. Fig. 12b shows the average B_0 field measured as a function of depth. At a depth of 5 mm, we have a field strength of $\approx$

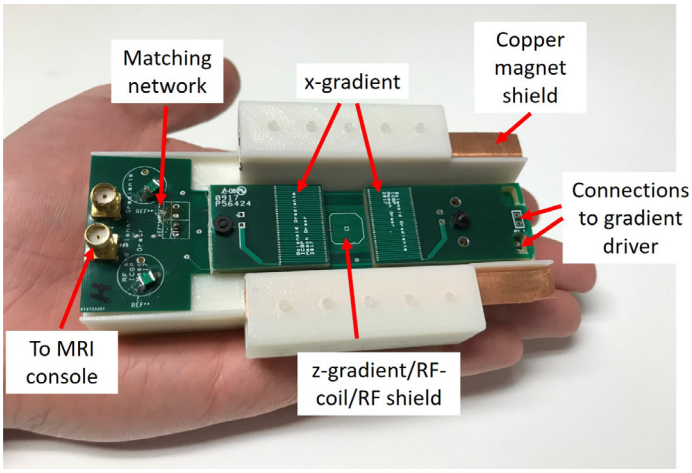

Fig. 11. A completely-assembled hand-held MRI sensor.

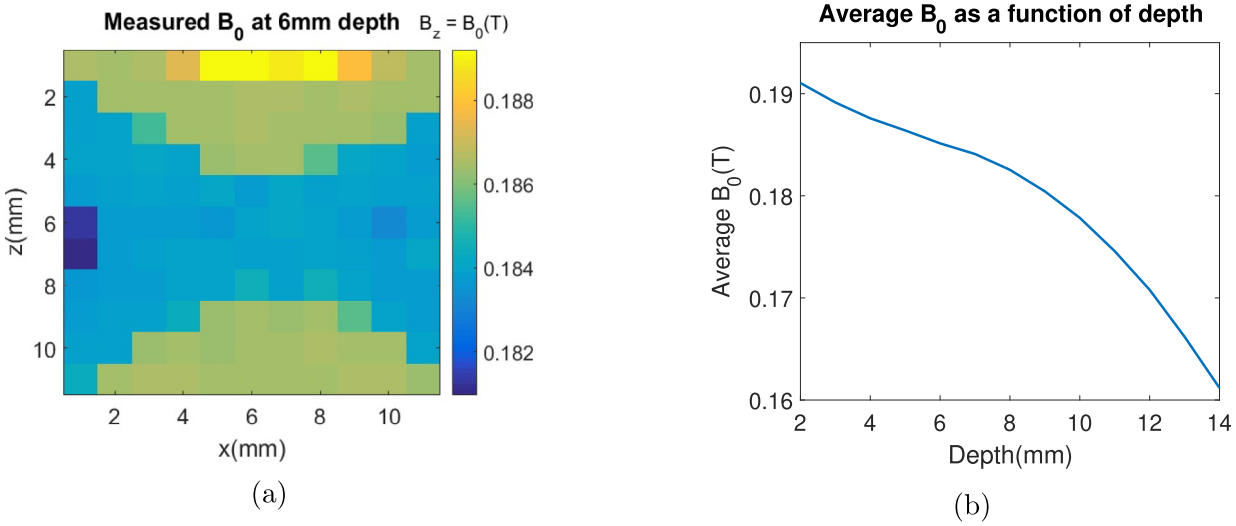

Fig. 12. (a) Measured B_0 field at a depth of 6 mm above the RF coil. The field is measured along the profile of the RF coil. (b) Plot of the magnitude of B_0 as a function of depth. The measured gradient strength at a depth of 5 mm is $\approx$ 2.2 T/m.

0.1859 T and a gradient strength of $\approx$ 2.2 T/m; the latter is in good agreement with simulations.

One potential reason for the differences between measured and simulated B_0 values is mismatch between the magnets. As quoted by the vendor (K&J magnetics), N52 magnets can have a residual flux density B_r that varies between 1.45 and 1.48 T, i.e., by $\pm$1%. In addition, B_r can vary significantly in magnitude and direction within the volume of a given magnet. We quantified such variability by measuring the on-axis magnetic fields on the surfaces of two separate magnets, and found that they (i) differed on average by 1.6% between magnets, and (ii) varied by 1.5% (rms) along the axis of each magnet. Such variability largely accounts for the observed differences between measured and simulated B_0 fields.

The RF coil was wound on two PCB layers with three turns per layer. Its properties were measured using an impedance analyzer and the results are summarized in Table 3. The extracted inductance and resistance are 534 nH and 2 Ω, respectively, resulting in $Q = 13.4$ at the typical Larmor frequency of 8.0 MHz. This value is about 2$\times$ lower than the "bare" coil; Q of the fully-assembled coil is lowered by eddy currents in the copper shield below the RF coil. Several slotted shields were designed and tested, but did not provide a significant improvement in Q.

Table 3
Summary of the RF coil characteristics at 8 MHz.

Turns per layer	Number of layers	Resistance	Inductance	Q
3	2	2 Ω	534 nH	13.4

The strength of the static gradient G_0 was verified by conducting a 2D diffusion-T_2 correlation NMR experiment on a doped water sample. The pulse sequence for this experiment in shown in Fig. 13a. The measured signal is given by

$$s(t,\tau_1) = \int\int f(T_2,D)e^{-2/3\gamma^2 G_0^2 \tau_1^3} e^{-t/T_2} dT_2 dD, \quad (9)$$

where τ_1 is the encoding period, as before. The experiment is run for multiple values of τ_1, and the D-T_2 correlation distribution is then estimated by (i) assuming G_0 is equal to its predicted value of 2.2 T/m at a depth of 5 mm; and (ii) using a 2D inverse Laplace transform (ILT) as described by [20]. Fig. 13b shows the measured D-T_2 correlation distribution of the doped water sample. The horizontal dashed line in the figure shows the known diffusion coefficient of water at room temperature, which is in excellent agreement with

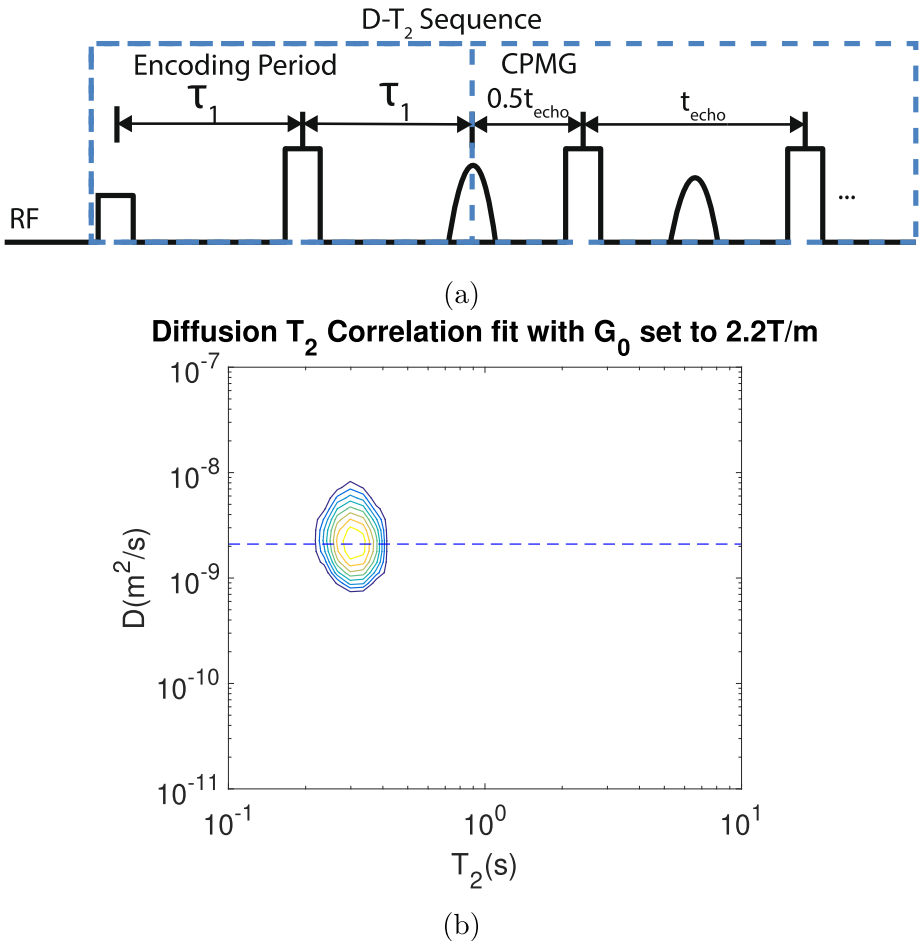

Fig. 13. (a) The pulse sequence used for the D-T_2 correlation experiment. (b) The measured D-T_2 correlation distribution for doped water assuming $G_0 = 2.2$ T/m.

the mean value of the measured D-T_2 distribution along the diffusion axis. This result confirms that the measured value of G_0 is in good agreement with simulations.

3.2. Minimizing the dead time

In order to minimize the value of $t_{E,min}$, the total dead time of the probe after each RF pulse must be minimized. Following [14], copper shields were used to prevent magneto-acoustic ringing from occurring in the magnets, no magnetic components were used on the PCB, and all the PCBs were rigidly attached to the housing in order to minimize vibrations after strong RF or gradient pulses.

We compared the difference in ringdown after an RF pulse between a sensor that is not properly shielded and also contains magnetic components (Fig. 14a) with a properly shielded sensor that does not contain any magnetic components (Fig. 14b). The ringdown visible in Fig. 14a is due to both a poorly-shielded magnet and also induced vibrations of nickel-plated jumper pins in the matching network. These vibrations propagate through the entire PCB, causing the RF coil to vibrate as well. Furthermore, because nickel is ferromagnetic, the vibrations also cause small perturbations in the B_0 field. To quantify the ringdown, we fit an exponential function to the measured waveform, resulting in an extracted time constant of 175 μs. Such a long ringdown period is unacceptable for collecting data with short echo spacing. Fig. 14b shows ringing on the same sensor with proper shielding and without the nickel-plated jumper pins. In this configuration, the ringdown ends in approximately 10 μs, allowing us to collect data with very short echo spacing.

To illustrate the short dead time and thus low values of $t_{E,min}$ that were achieved, we used CPMG sequences to measure the T_2 decay of the dielectric substrate material (FR-4) used in the PCBs. Sequences with $t_E = 30$ μs were used to measure the rapid relaxation rate expected for such a rigid solid. Fig. 15 shows the measured transverse relaxation of the FR-4 both with and without an additional PCB placed on top of the RF coil. Fig. 15a displays the two decay curves. The amplitude of the signal with added FR-4 material is larger than without the added material, as expected. To confirm that both signals have the same decay, we normalize each decay curve and plot them on top of each other as shown in Fig. 15b. In both cases, the T_2 decay is bi-exponential with components at 0.3 ± 0.03 ms and 12 ± 1.01 ms, which strongly suggests that the measured background signal (without the additional PCB) is generated by FR-4. The bi-exponential decay may arise from the fact that FR-4 is a composite material composed of woven fiberglass cloth with an epoxy resin binder; these components likely give rise to the short- and long-T_2 components, respectively.

3.3. RF shield performance

The effectiveness of the shield used to reduce external noise pickup and decouple noisy samples from the RF coil is quantified in this section. In particular, we quantified the effectiveness of the shield by placing a finger on both a shielded coil and an un-

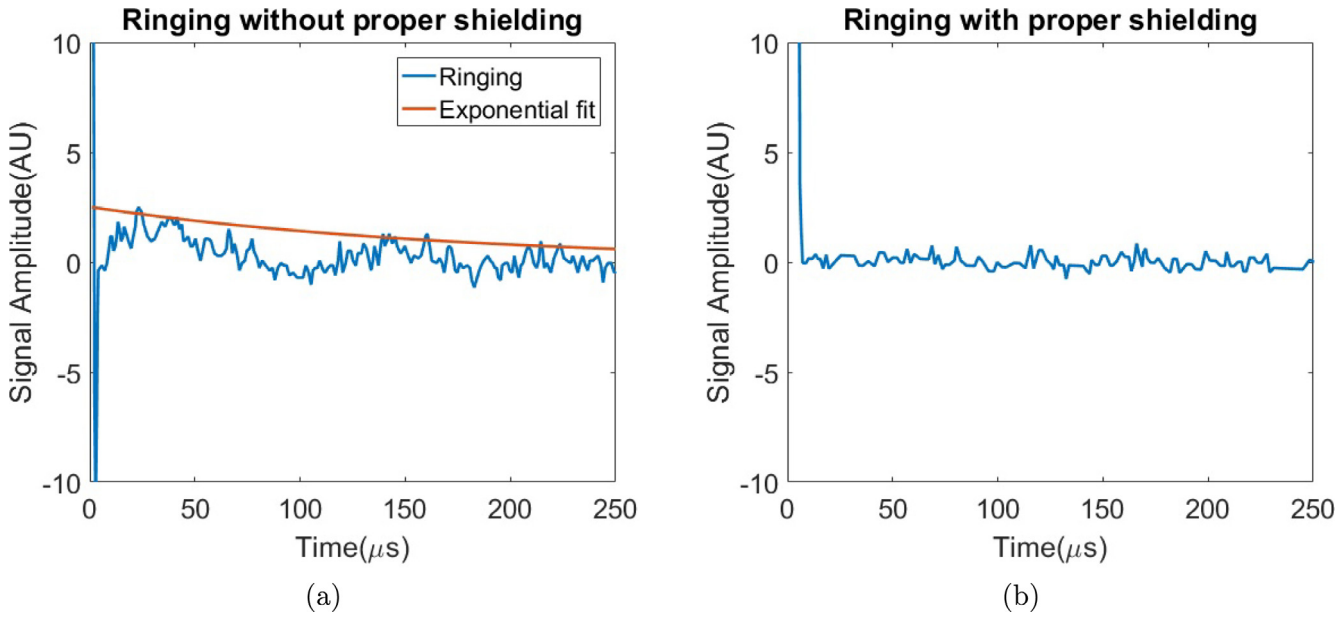

Fig. 14. (a) Measured ringdown waveform after a 90° pulse for a sensor that is not properly shielded and also contains magnetic components. An exponential decay function was fit to the peaks of the waveform, resulting in an estimated time constant of 175 μs. (b) Same as (a), but for a sensor that is properly shielded and does not contain magnetic components. The ringdown quickly disappears (in about 10 μs).

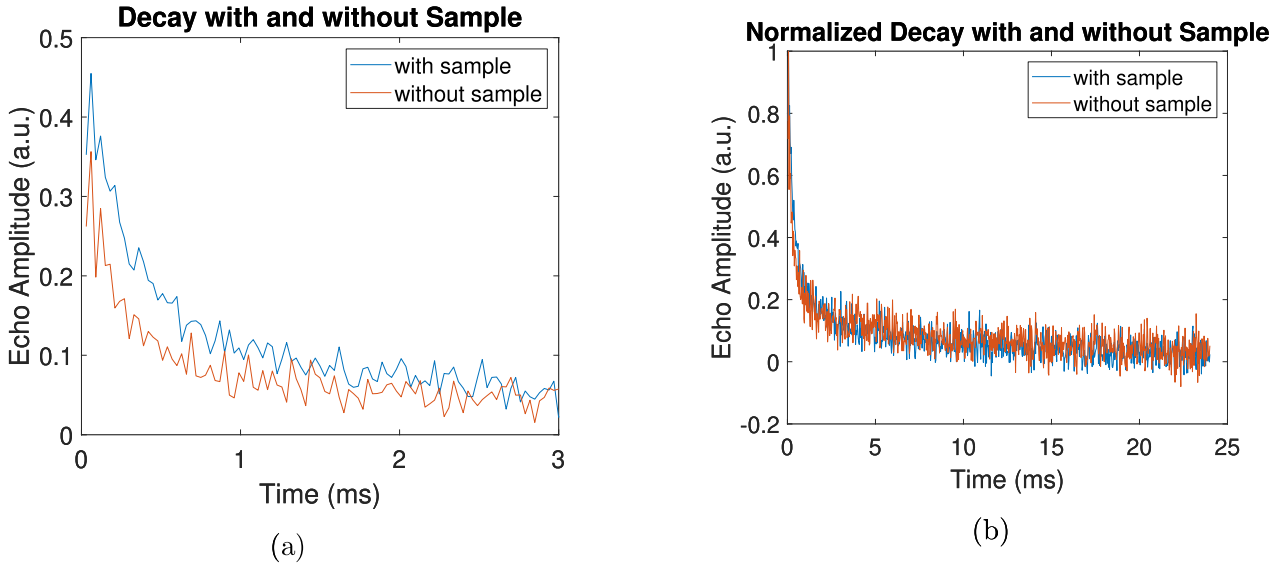

Fig. 15. Measured echo decay of PCB substrate material (FR-4) with and without an additional PCB (the "sample") placed on the RF coil. Both samples decay as bi-exponential functions with fitted T_2 components of 0.3 ± 0.03 ms and 12 ± 1.01 ms. (a) Raw echo decay curves measured with and without the additional PCB. The amplitude of the signal with sample is 0.4 ± 0.03 (a.u.) and the amplitude without sample is 0.3 ± 0.03 (a.u.). (b) Same data as in (a), but after normalization of the amplitudes. Both curves decay at the same rate (within statistical error), suggesting that the signals measured without the additional PCB arise from the FR-4 substrate of the RF coil PCB.

shielded coil. Fig. 16 shows the noise spectra recorded in both cases, compared to the baseline (i.e., without the finger present). The total rms noise increases by only 11.94% for the shielded coil, compared to 173.13% for the un-shielded coil. This result shows that the shield greatly reduces external noise pickup, as expected, and is thus extremely important if one wants to collect data on large biological samples outside of a shielded room.

3.4. Sample heating

The strong RF pulse trains (typical peak power of 63.1 W) used in this sensor will generate significant eddy currents and Joule heating within conductive samples. The resulting temperature rises have the potential to cause sample damage (e.g., due to tissue burns or melting). We characterized this effect by measuring the temperature rise of a heavily-doped water sample ($T_2 \approx 100$ ms) after applying a CPMG pulse train. In particular, we first measured the temperature of the sample using a digital laser-guided infrared thermometer. Then we conducted a CPMG pulse sequence with typical parameters used during imaging (1000 echoes, an echo spacing of $t_E = 100$ μs, an inter-experimental time of 200 ms, and 256 averages). After the experiment, we measured an increase in sample temperature of 4.8 °C (from 22.5 °C to 27.3 °C), which is significantly larger than recommended for tissue.

To reduce the amount of heating, the RF power levels must be decreased. However, decreasing the power level will also reduce

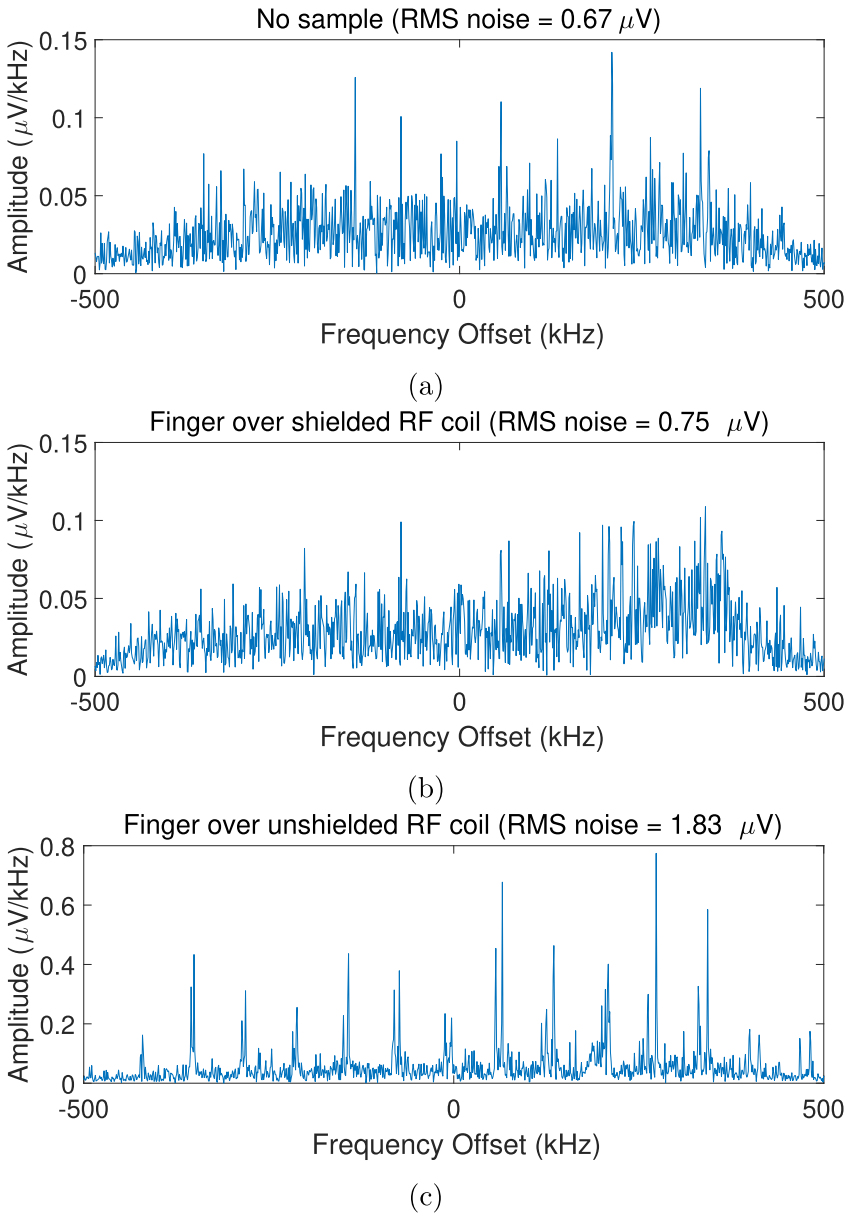

Fig. 16. Comparison of noise spectra measured with (a) no sample placed on the RF coil, (b) a finger placed on a shielded RF coil, and (c) a finger placed on an un-shielded RF coil.

SNR due to (i) decreased slice thickness, and (ii) increased RF pulse length (resulting in increased t_E and fewer echoes per unit time). We believe that composite excitation and refocusing pulses offer a promising method for reducing the RF power level while maintaining similar values of SNR [21,22]; these will be studied in future work.

4. Imaging results

4.1. Effects of B_0 and B_1 inhomogeneity

As a consequence of keeping the sensor as small as possible, the B_0 and B_1 profiles are not completely uniform within the FOV, as described in Section 2. The inhomogeneous B_0 profile results in excitation of the sample at slightly different depths across the FOV, while the inhomogeneous B_1 profile results in a non-uniform flip angle across the sample. Together, these two effects result in a non-uniform sensitivity profile across the image.

To study the sensitivity profile, we image a uniform sample that was larger then the sensor's FOV (which is limited by the RF coil to approximately 9 mm $\times$ 9 mm). The uniform sample in this case was a 10 mm NMR tube filled with doped water. Fig. 18a shows the measured image of the sample. We will refer to this image as the reference image, $R(x,z)$. The intensity profile is clearly non-uniform, with a bright horizontal line extending across the center of the FOV, which is in agreement with the measured B_0 profile shown in Fig. 12a. We also see a loss in signal along the edge of the bright horizontal line, which is probably a consequence of the rapid drop in field in this region also visible in Fig. 12a.

The measured $R(x,y)$ shown in Fig. 18a can be used to correct for the non-uniform sensitivity profile of the sensor. For this purpose, acquired images must be divided by $R(x,y)$. Since noise in the reference degrades SNR of the corrected images, we averaged $R(x,y)$ over significantly more scans (32 in this case) than a typical imaging experiment. A small offset was also added to $R(x,y)$ in the region outside the FOV; this limits the noise amplification due to division by values close to zero. We also suppress amplification

that still occurs by multiplying the corrected images with a function $P(x,y)$ that suppresses noise outside the FOV. In particular, we create $P(x,y)$ by thresholding a 2D circularly-symmetric Gaussian function, thus ensuring it remains a constant value within the FOV but gradually falls off to 0 outside of the FOV. As a result, the noise suppression operation has no effect on the actual image within the FOV but suppresses the noise outside of the FOV.

To test this method, we collected an image of a 10 mm NMR tube filled with (i) doped water, and (ii) two 3 mm NMR tubes filled with doped water. One 3 mm tube was placed slightly off-center, while the other was placed at the corner of the FOV as shown in Fig. 17. By default, we set the size of the acquired images to 41×41, which in our case resulted in a good compromise between resolution and total scan time. The maximum gradient current was limited to 10 A to prevent damage to the PCB traces, while the default slice thickness (limited by the available RF power level) was approximately 0.7 mm. Other pulse sequence parameters are summarized in Table 4. Note that the refocusing pulses (denoted by 180°) are significantly shorter than twice the length of the excitation pulse (denoted by 90°), even though they have the same RF power level. This is because the optimal ratio of excitation to refocusing pulse length that maximizes SNR in grossly inhomogeneous fields is known to vary between 1.4 and 1.6 [21].

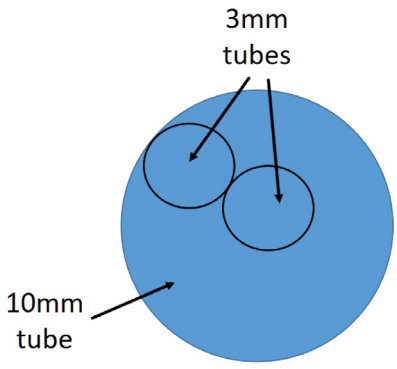

Fig. 17. Schematic of the test sample measured during the sensitivity correction experiment. All of the tubes were filled with doped water.

We confirmed this fact by conducting a pulse length sweep, resulting in optimal pulse lengths of 13 and 18 μs (which are in a ratio of ~1.4) for the excitation and refocusing pulses, respectively.

During the experiments, the center pixels of k-space were measured first, followed by an outward spiral pattern to cover the rest of k-space. This pattern was used because the most visually-important information in typical images resides at low spatial frequencies, i.e., within the center pixels. Thus, the chosen sampling pattern minimizes the visual effects of temperature variations during the experiment. The acquired k-space data was zero-padded to generate 256×256 matrices and the inverse Fourier transform was then used to construct images; note that zero-padding helps to smooth the images.

Fig. 18b shows the measured image of the test sample (two 3 mm NMR tubes placed inside a 10 mm NMR tube, with all tubes filled with doped water). The expected non-uniform intensity profile is clearly visible in the image. We then use the procedure described above, in which we divide Fig. 18b by the reference image $R(x,y)$, to find the corrected image shown in Fig. 18c. Visual inspection of Fig. 18c confirms that the intensity within the FOV is significantly more uniform, as expected. Note that we are able to resolve the ~0.27 mm thick walls of both 3 mm NMR tubes even without correcting for field inhomogeneity.

4.2. Images of 3D-printed phantoms in doped water

In order to highlight the capabilities of the proposed sensor, we acquired images of phantoms that were created using 3D-printed plastic pieces immersed in doped water. For this purpose, a 10 mm NMR tube was filled with $CuSO_4$ solution (with measured $T_2 \approx 60$ ms), and 3D-printed objects (e.g., cylinders with letter-shaped cutouts) were then inserted into the tube. Pulse parameters for these experiments are summarized in Table 5. Note that we choose relatively conservative values for the echo period t_E in order to verify that the system still preforms well under non-optimal conditions (e.g., in field environments).

Fig. 19 shows the measured images for four letter-shaped 3D-printed phantoms. A total of $N = 8$ scans were acquired for the letters "C", "W", and "U", resulting in a total experimental time of ~54 min for both the x and y experiments in each case. In addition, $N = 16$ scans were acquired for the letter "R" to verify whether

Table 4
Default pulse parameters used for the imaging experiments.

Frequency	Depth	RF power	90° length	180° length	G_z length	G_x length	t_E	N_E
7.92 MHz	6 mm	63.1 W	13 μs	18 μs	345 μs	450 μs	100 μs	1200

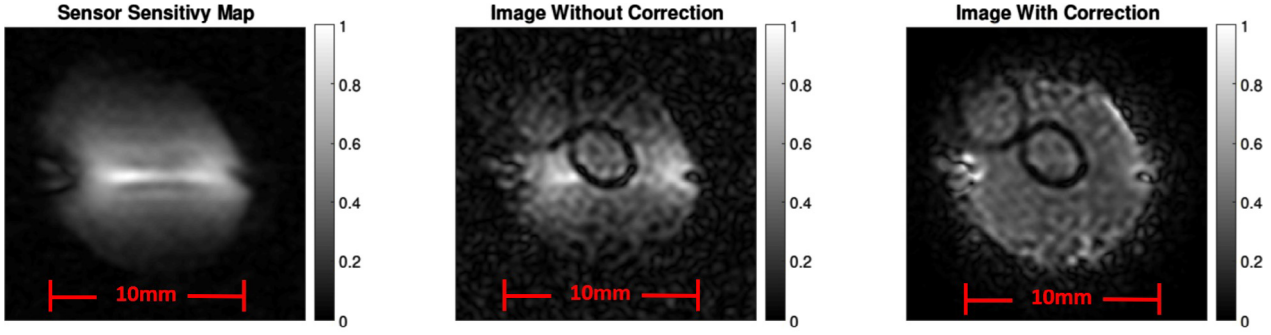

Fig. 18. (a) Measured image of a uniform sample (a 10 mm tube filled with doped water). This data is used to define the sensor's reference map $R(x,y)$. (b) Image of two 3 mm tubes (filled with doped water) placed inside of a 10 mm tube (also filled with doped water). The expected intensity profile $R(x,y)$ can be seen in the background of the image. (c) Corrected version of (b), which has a much more uniform background.

Table 5
Pulse parameters for images of 3D-printed phantoms.

Frequency	Depth	RF power	90° length	180° length	G_z length	G_x length	t_E	N_E
7.93 MHz	6 mm	63.1 W	13 μs	18 μs	225 μs	500 μs	200 μs	200

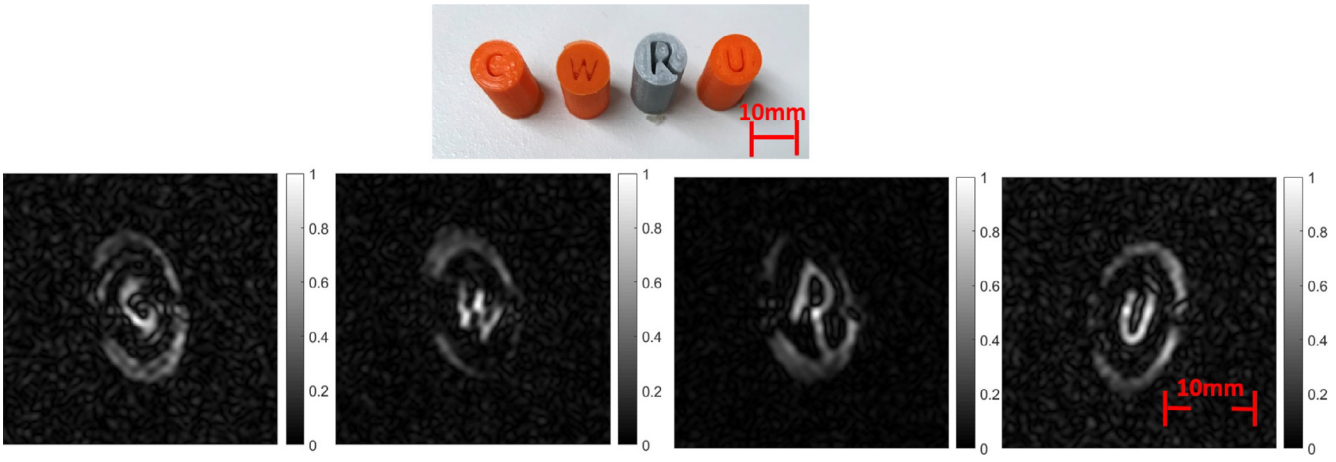

Fig. 19. (Top) Photographs of the 3D-printed phantoms. All phantoms are made of the same material, but the "R" phantom was printed in a different color. (Bottom) Images of the phantoms, as acquired by the proposed hand-held MRI sensor using the parameters listed in Table 5. (For interpretation of the references to colour in this figure legend, the reader is referred to the web version of this article.)

$SNR \propto N^{1/2}$ as expected for uncorrelated noise sources. Deviations from this relationship indicate one or more correlated error sources, such as temperature drift of the magnets during long experiments. Also note that while the "R" phantom has a different color from the other letters, it is actually made of the same material (ABS). In each case, the doped water present in the letter-shaped cutouts is clearly visible, as is additional water around the edges of the FOV. Note that the wait time t_W for these experiments was set to be much longer than T_1, thus resulting in images that have mainly spin density and T_2 contrast. The image resolution is ~0.3 mm over a 25 mm FOV, but can be further improved by increasing the peak gradient strength (either by using longer gradient pulses and/or more current).

We estimate the SNR of the images by first selecting a region of interest (ROI) in the image that is within the sample. We then select a ROI in a region outside of the sample and calculate the standard deviation of that portion of the image. From these two values, we calculate the SNR per scan as

$$SNR/scan = \frac{mean(s)}{\sigma\sqrt{N}}, \tag{10}$$

where s denotes pixels of the ROI that is located within the sample, σ is the standard deviation of the noise (for the ROI that is located outside the sample), and N is the number of scans used to calculate the SNR/scan. Based on this equation, we get an SNR/scan of approximately 10 for all four images collected.

4.3. T_1-weighted images

In another example, we acquired T_1-weighted images of a sample consisting of a 3 mm NMR tube filled with tap water ($T_1 \approx 2000$ ms) inside a 10 mm NMR tube filled with doped water ($T_{1,doped} \ll T_{1,tap}$). We acquired data following the procedure outlined in Section 2.6, with $t_W = 200$ ms. The pulse parameters for this experiment are summarized in Table 5.

Fig. 20a shows the measured echo decays of the doped and tap water samples. As expected, they have the same initial amplitude. The estimated T_2 from the tap water curve is 600 ms and the estimated T_2 from the doped water curve is 200 ms. The effect of diffusion is also clear since the effective decay time constant $T_{2,eff}$ of the tap water is 600 ms instead of the expected ~2000 ms. Because $T_1/T_2 \approx 1$ for both tap and doped water, we assume that $T_{1,doped} \ll T_{1,tap}$. If special steps are not taken to ensure T_1 weighting, the resulting image will show a mixture of T_1, T_2, and D contrast that will be increasingly dominated by T_2 and D as we add up more echoes. By collecting only the first few echoes (i.e., such that $N_E t_E < T_{2,eff}$), we can reduce the contrast due to T_2 and D.

The resulting T_1-weighted image is shown in Fig. 20b; note that the intensity profile has been corrected using the method described in Section 4.1. The bright background of the corrected image corresponds to the doped water, while the dark circle corresponds to the tap water, as expected. The methods used to acquire and process this image can be applied to any sample with different T_1 components.

4.4. Imaging of food products

QA of food products is of the utmost importance for both safety and quality. Imaging is becoming a popular and capable method for QA of this purpose [23]. In particular, the use of NMR and MRI for QA has been discussed previously [24–26]. However, they are relatively uncommon in industrial applications.

One of the most consumed beverages in the world is coffee and its quality is extremely important. Due to this fact, methods for monitoring how processing and storage affect the quality of coffee are also important. One promising method is to study the internal structure of coffee beans over time. Synchrotron radiation microtomography has been used to study the internal structure of coffee beans both before and after roasting [27]. Single-sided MRI sensors can offer a complementary method. We demonstrated their utility by acquiring images of roasted coffee beans at two different depths

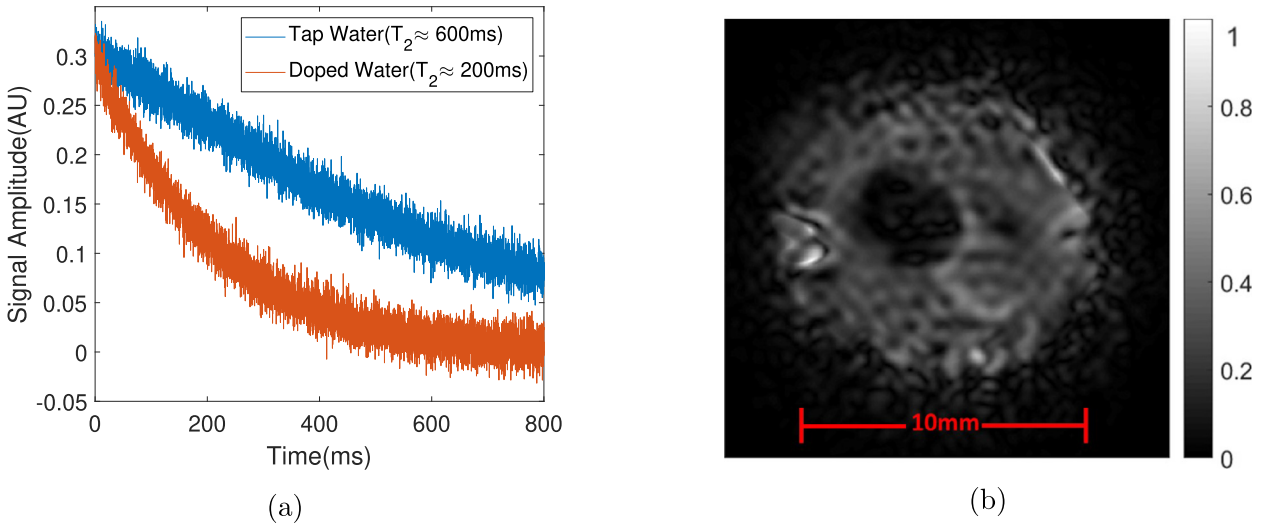

Fig. 20. (a) Measured T_2 decay of the doped and tap water samples. It is clear that the two have the same initial amplitude but different decay rates. (b) Measured T_1-weighted image of a 3 mm NMR tube filled with tap water and placed within a 10 mm NMR tube filled with doped water ($T_{1,doped} \ll T_{1,tap}$).

as shown in Fig. 21. Due to the beans being roasted, much of their internal moisture had evaporated, resulting in low signal amplitudes and poor SNR. Nevertheless, we acquired two images at different depths within a single bean. The first slice has a larger cross-section (near the bottom of the bean) as shown in Fig. 21a, while the second has a smaller cross-section (near the top of the bean) as shown in Fig. 21a. Moreover, it is clear that the cross-section is more circular towards the top of the bean with a diameter of $\approx$ 5 mm. The bottom slice shows an oval with a major axis diameter $\approx$ 10 mm and minor axis diameter $\approx$ 5 mm. Currently, these images do not have enough SNR to accurately resolve any internal structure of the beans. However, further improvements in single-sided MRI have the potential to enable such measurements. Moreover, we can still extract transverse relaxation rates from the pixels located within the coffee bean. The result from Fig. 21 is a mono-exponential with $T_{2,eff} \approx 68$ ms, which is somewhat shorter than the value of 92 ms measured from the same sample using a CPMG sequence. The difference is probably due to the fact that the asymptotic echo shapes in the imaging pulse sequence (see Fig. 10) and the CPMG arise from a different mixture of coherence pathways [28]. The diffusion sensitivity of these pathways can vary significantly, thus resulting in different values of $T_{2,eff}$ (and in general, multi-exponential decay curves).

As a control, we imaged the same beans using a conventional 0.5 T permanent magnet-based MRI system (NIUMAG NMI20). Two slices of three coffee beans arranged along the bore of the magnet are shown in Fig. 22. These results are broadly similar to those obtained with the hand-held sensor. For example, they confirm that the cross-sections of the beans are oval near the bottom and become increasingly circular towards the top. In this scenario, the top bean in Fig. 22a has a major axis diameter $\approx$ 10 mm and minor axis diameter $\approx$ 7 mm and the top bean in Fig. 22b has a diameter $\approx$ 5 mm. These results are in agreement with those obtained from the single-sided sensor.

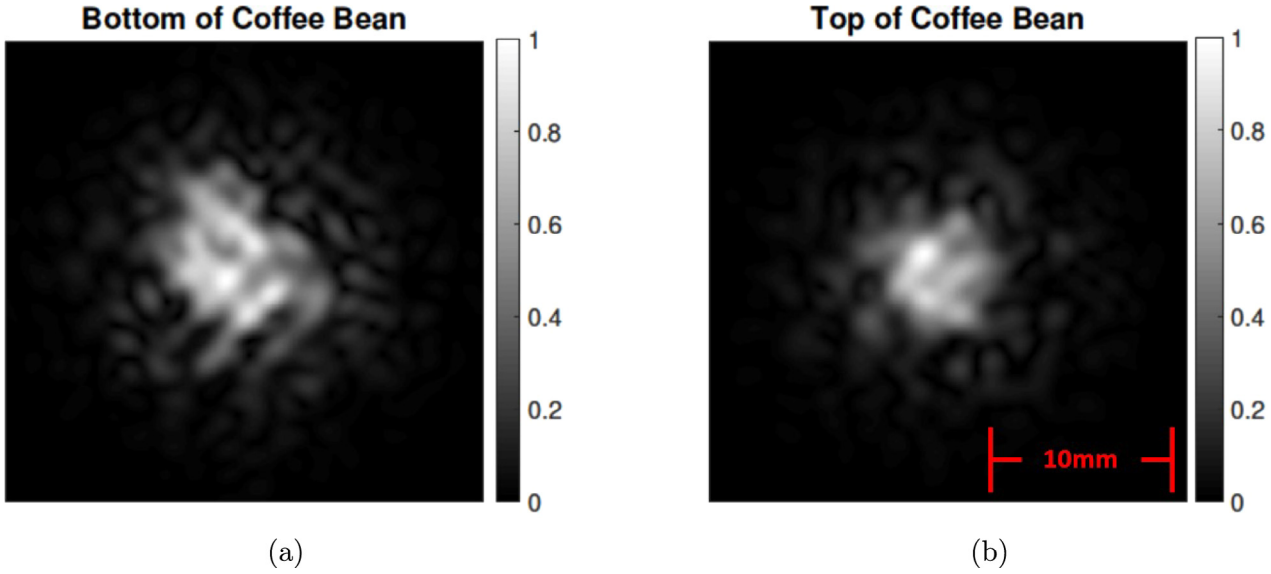

Fig. 21. Measured images of a coffee bean acquired by the single-sided sensor: (a) bottom slice, and (b) top slice. The bottom slice shows an oval shape for the coffee bean with major axis diameter $\approx$10 mm and minor axis diameter $\approx$5 mm. By contrast, the top slice shows a circular shape with diameter $\approx$5 mm.

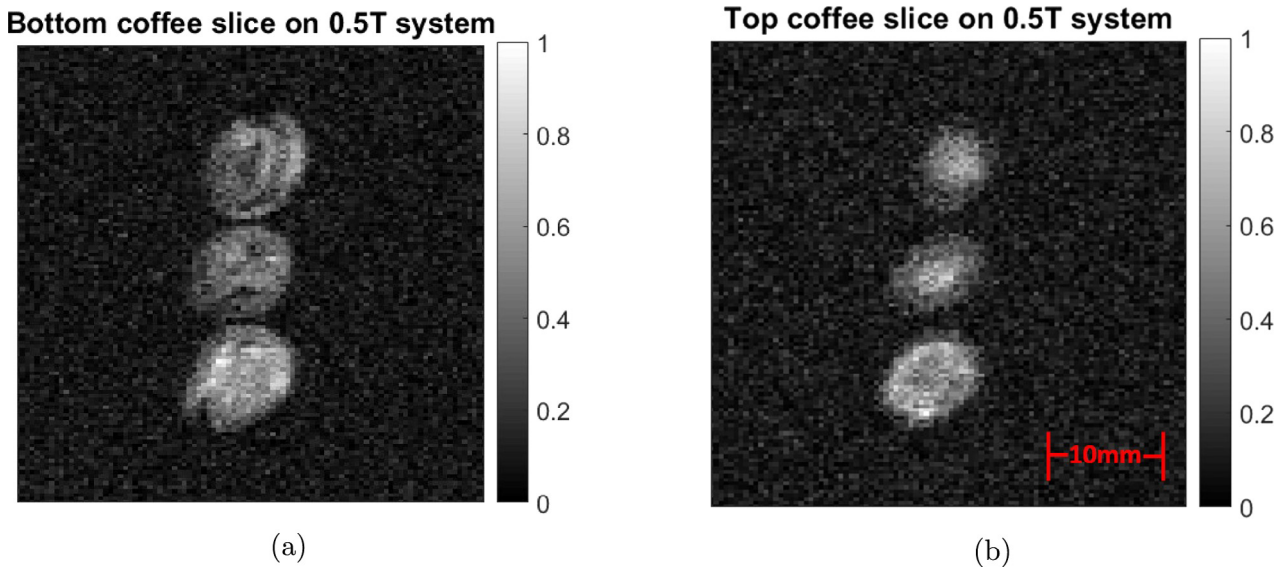

Fig. 22. Measured images of a coffee bean acquired by a conventional 0.5 T system (NIUMAG NMI20): (a) bottom slice, and (b) top slice. The scale bars for both (a) and (b) are identical.

Another potential application for the proposed device is for QA of pitted fruits. The process of removing the pit of a fruit is usually based on using a mechanical plunger to push the pit out of the fruit. In some cases, the pit is not fully removed. Being able to detect fruits in which the pit was not fully removed is crucial to the quality of the final product [29,30]. MRI is a good candidate for this process and a low-field imaging system coupled with image recognition algorithms could be used in the future to both detect and locate left-over pits. Furthermore, relaxation parameters can be extracted from the images to provide more chemical information such as water and oil content that can further be used to improve processing and storage of the food products.

Because of this, we collect images from a canned, sliced black olive. Olives have much higher water content than roasted coffee beans, resulting in images with higher SNR. Fig. 23a shows a slice of the olive collected with the handheld sensor, while Fig. 23b shows a photograph. The image looks slightly different from the photograph due to the fact that we are measuring a slice located inside the olive. However, the general structures are similar.

Similar to the coffee bean, we also extract transverse relaxation rates from the pixels located within the olive in Fig. 23a. In this case, the measured curves are bi-exponential functions with average decay time constants of $T_{2a} = 7.3$ ms and $T_{2b} = 73$ ms. CPMG sequences also result in bi-exponential decays, but with somewhat longer time constants ($T_{2a} = 18$ ms and $T_{2b} = 116$ ms) as expected based on the earlier experiment.

In this section, we introduced potential applications for single-sided MRI sensors in the food industry, in particular to provide useful information for QA of coffee beans and pitted fruits. We hope that the preliminary results presented here will motivate further improvements in sensor and pulse sequence design.

5. Comparison to other single-sided MRI sensors

Table 6 compares the work described in this paper with other single-sided MRI sensors published in the literature [3,6,4]. The table lists the size, depth of investigation (DOI) referred to the sensor surface, static gradient (G_0), sensitive region for 2D imaging,

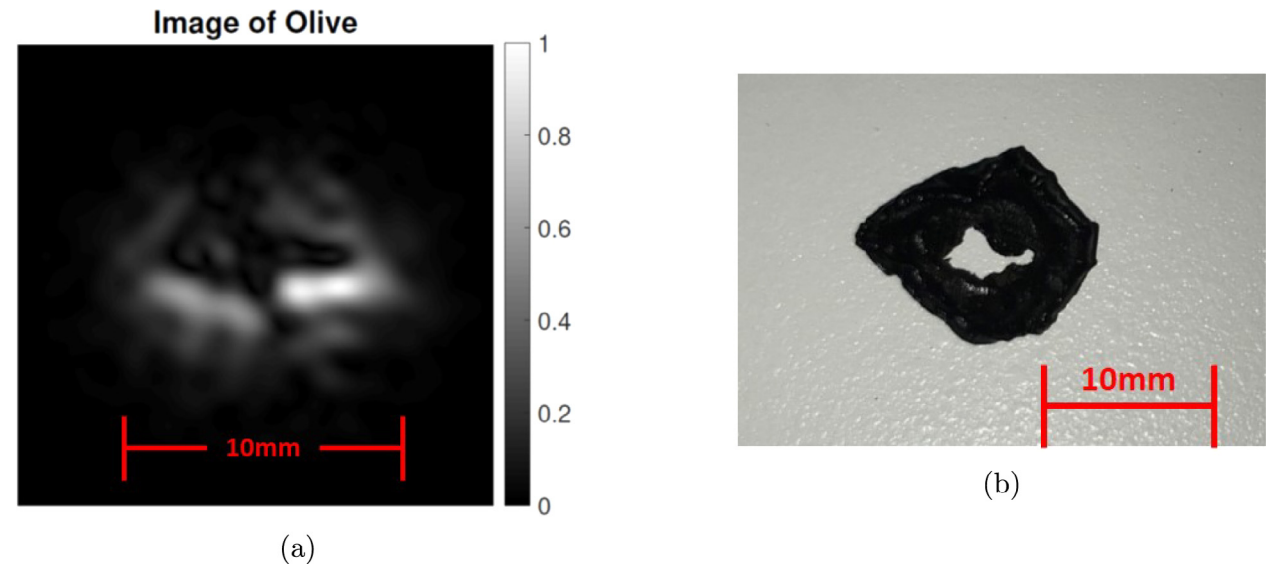

Fig. 23. (a) Cross-section of a sliced olive acquired with the hand-held sensor. (b) A photograph of the same sample.

Table 6
Comparison to similar work.

Reference	Size ($L \times W \times H$ (mm^3))	DOI (mm)	G_0 (T/m)	Sensitive region (mm^2)	SNR/scan
This work	$117 \times 85 \times 30$	6	2.2	9×9	10
Casanova et al. [3]	$45 \times 40 \times 20$	1	16.6	10×10	2.3
Zhonghua et al. [6]	$166 \times 164 \times 69$	3	7.46	10×10	4
Perlo et al. [4]	$300 \times 300 \times$ N/A	2–10	2.5	36×26	20 (DOI = 6 mm)

and the SNR per scan of each system. Note that the SNR per scan was not reported in previously-published work, even though it is an important performance metric for a practical imaging system. Thus, we downloaded one or more images from the corresponding papers and calculated the SNR/scan ourselves by using Eq. (1).

Of the three other systems described, the only sensor more compact than that designed in this work is from [3]. One main difference between the system in [3] and that described in this paper is that the sensor in [3] consists of only one magnet to generate the B_0 field. Such a geometry keeps the sensor very compact at the expense of a very strong static gradient. A significant improvement in this work over [3] is the reduction in the static gradient strength by almost factor of 8. As described earlier, this increases the SNR per unit bandwidth of the RF pulses and reduces losses due to diffusion. The reduction in G_0 allows imaging at greater depths while maintaining a higher SNR/scan than what is described in [3]. Note that a single-echo pulse sequence is used in [3], which obviously eliminates averaging over multiple echoes per scan. Therefore, a combination of i) reduced G_0, and ii) use of multi-echo pulse sequences allows our sensor to image at much greater depths while maintaining a high value of SNR/scan.

Another difference between this work and [3] is the construction of the sensor itself. From [3], it is not clear how the system is assembled. However, it appears that the overall construction of the housing will require the use of some level of machining to properly secure the magnets and connectors. By contrast, our system does not require any machining, which makes it simple to construct.

The work described in [6] is both larger in size and also has a larger static gradient than our system. The larger G_0 will contribute to a smaller SNR and make imaging at greater depths more difficult. In fact, we achieved a higher SNR/scan at a deeper DOI than in this work. Furthermore, the system in [6] is constructed with hand-wound RF and gradient coils, making its construction more difficult. Also, the machining tolerances of the housing cause significant errors in the overall B_0 field. The 3D-printed housing used in our design has very tight tolerances (< 20 μm), which helps to reduce such field generation errors.

Finally, the system described in [4] is much larger than the design we present here. However, the added size allows for a much larger FOV while maintaining a similar G_0 strength as our system. The DOIs studied in [4] also vary over a broad range (2–10 mm). The larger magnet design increases the B_0 strength, which allows the RF coil to be placed further away from the magnets. This can eliminate the need to shield the magnets from strong RF pulses. Without the shield, the RF coil will not suffer the penalty of lower Q, unlike our sensor. The larger sensor design also allows for a larger RF coil, resulting in improved sensitivity over the desired FOV. Thus, the system in [4] has double the SNR/time at a comparable depth of 6 mm, but at the cost of a much larger sensor. Another advantage our sensor has over that described in [4] is ease of construction. As with many other systems, the gradients in [4] are hand-wound, which can be time consuming. Also, special assembly methods are required for properly mounting the gradients, unlike in our system where the PCBs simply lie flat on top of each other (see Fig. 6).

6. Summary and conclusions

This work has described the design, development, and testing of an easily manufactured, low-cost, hand-held, and single-sided MRI sensor. The sensor is made of a 3D-printed housing and PCBs that allow for easy optimization of the geometry and excellent reproducibility. The relevant design files have been uploaded to an online repository to help others who want to enter the field of single-sided MRI. The sensor has been used to successfully acquire images in 108 min with a 0.33 mm resolution over a FOV of 9×9 mm. The SNR per scan of these images collected was measured to be approximately 10 per scan. The imaging time can be significantly reduced by reducing the resolution.

We hope that the simple design and construction of the proposed sensor will help to reduce the barrier to entry for others interested in using single-sided NMR and MRI for their own applications as well as to increase research in the field. The proposed sensor has relatively low SNR per scan, and thus requires long imaging times. However, the addition of advanced methods such as compressed sensing, rapid re-tuning of the probe (to allow multiple slices to be measured within the same scan), redesign of the RF coil to improve sensitivity, and implementation of broadband composite pulses may help to significantly increase the overall SNR per scan [31–33]. Furthermore, high quality quantitative T_1 and diffusion coefficient images are also possible by encoding the T_1 and diffusion values in the echo shape itself [34].

Acknowledgments

The authors would like to acknowledge the help of Dr. Michael Twieg, who designed an earlier version of the sensor. The authors also would like to acknowledge the National Science Foundation (NSF) for funding support. This work was partially funded by the NSF through grant CCF-1563688.

References

[1] Mayu Nakagomi, Michiru Kajiwara, Jumpei Matsuzaki, Katsumasa Tanabe, Sodai Hoshiai, Yoshikazu Okamoto, Yasuhiko Terada, Development of a small car-mounted magnetic resonance imaging system for human elbows using a 0.2T permanent magnet, J. Magn. Reson. 304 (2019) 1–6.
[2] G. Eidmann, R. Savelsberg, Peter Blümler, Bernhard Blümich, The NMR MOUSE a mobile universal surface explorer, J. Magn. Reson. 122 (1996) 104–109.
[3] F. Casanova, B. Blümich, Two-dimensional imaging with a single-sided NMR probe, J. Magn. Reson. 163 (1) (2003) 38–45.
[4] J. Perlo, F. Casanova, B. Blümich, 3D imaging with a single-sided sensor: an open tomograph, J. Magn. Reson. 166 (2) (2004) 228–235.
[5] Lina A. Colucci, Kristin M. Corapi, Matthew Li, Xavier Vela Parada, Andrew S. Allegretti, Herbert Y. Lin, Dennis A. Ausiello, Matthew S. Rosen, Michael J. Cima, Fluid assessment in dialysis patients by point-of-care magnetic relaxometry, Sci. Transl. Med. 11 (502) (2019).
[6] Zhonghua He, Wei He, Jiamin Wu, Zheng Xu, The novel design of a single-sided MRI probe for assessing burn depth, in: In Sensors, 2017.
[7] A. Guthausen, G. Zimmer, P. Blümler, B. Blümich, Analysis of polymer materials by surface NMR via the MOUSE, J. Magn. Reson. 130 (1) (1998) 1–7.
[8] B. Blümich, P. Blümler, G. Eidmann, A. Guthausen, R. Haken, U. Schmitz, K. Saito, G. Zimmer, The NMR-MOUSE: construction, excitation, and applications, Magn. Reson. Imag. 16 (5) (1998) 479–484.
[9] Ashvin Bashyam, Matthew Li, Michael J. Cima, Design and experimental validation of unilateral linear Halbach magnet arrays for single-sided magnetic resonance, J. Magn. Reson. 292 (2018) 36–43.

[10] C. Casieri, S. Bubici, F. De Luca, Self-diffusion coefficient by single-sided NMR, J. Magn. Reson. 162 (2) (2003) 348–355.
[11] Ulrike Holzgrabe, NMR Spectroscopy in Pharmaceutical Analysis, Elsevier, 2017.
[12] J. Thomas Vaughan, John R. Griffiths, RF Coils for MRI, John Wiley & Sons, 2012.
[13] I.P. Gerothanassis, Methods of avoiding the effects of acoustic ringing in pulsed Fourier transform nuclear magnetic resonance spectroscopy, Prog. Nucl. Magn. Reson. Spectrosc. 19 (3) (1987) 267–329.
[14] S. Anferova, V. Anferov, M. Adams, P. Blümler, N. Routley, K. Hailu, K. Kupferschläger, M.J.D. Mallett, G. Schroeder, S. Sharma, and B. Blümich. Construction of a NMR-MOUSE with short dead time. Concepts Magn. Reson., 15 (1) 15–25.
[15] T. Paul Callaghan, Principles of Nuclear Magnetic Resonance Microscopy, Oxford University Press on Demand, 1993.
[16] P. Elleaume, O. Chubar, and J. Chavanne. Computing 3D magnetic fields from insertion devices. In Proceedings of the 1997 Particle Accelerator Conference (Cat. No.97CH36167), volume 3, pages 3509–3511 vol 3, May 1997.
[17] Robert W. Brown, Y.-C. Norman Cheng, E. Mark Haacke, Michael R. Thompson, Ramesh Venkatesan, Magnetic Resonance Imaging: Physical Principles and Sequence Design, John Wiley & Sons, 2014.
[18] D.I. Hoult, Paul C Lauterbur, The sensitivity of the zeugmatographic experiment involving human samples, J. Magn. Reson. (1969) 34 (2) (1979) 425–433.
[19] M.D. Hürlimann, D.D. Griffin, Spin dynamics of Carr-Purcell-Meiboom-Gill-like sequences in grossly inhomogeneous B0 and B1 fields and application to NMR well logging, J. Magn. Reson. 143 (1) (2000) 120–135.
[20] Y.-Q. Song, L. Venkataramanan, M.D. Hürlimann, M. Flaum, P. Frulla, C. Straley, T1–T2 correlation spectra obtained using a fast two-dimensional laplace inversion, J. Magn. Reson. 154 (2) (2002) 261–268.
[21] Soumyajit Mandal, Van D.M. Koroleva, Troy W. Borneman, Yi-Qiao Song, Martin D. Hürlimann, Axis-matching excitation pulses for CPMG-like sequences in inhomogeneous fields, J. Magn. Reson. 237 (2013) 1–10.
[22] Van D.M. Koroleva, Soumyajit Mandal, Yi-Qiao Song, Martin D. Hürlimann, Broadband CPMG sequence with short composite refocusing pulses, J. Magn. Reson. 230 (2013) 64–75.
[23] Quansheng Chen, Chaojie Zhang, Jiewen Zhao, and Qin Ouyang. Recent advances in emerging imaging techniques for non-destructive detection of food quality and safety. TrAC Trends in Analytical Chemistry, vol. 52, pp. 261–274, 2013. Modern Food Analysis and Foodomics..
[24] Mason Greer, Cheng Chen, Soumyajit Mandal, Automated classification of food products using 2D low-field NMR, J. Magn. Reson. 294 (2018) 44–58.
[25] Christopher J. Clark, Janet S. MacFall, Quantitative magnetic resonance imaging of 'fuyu' persimmon fruit during development and ripening, Magn. Reson. Imag. 21 (6) (2003) 679–685.
[26] A.K. Thybo, H.J. Andersen, A.H. Karlsson, S. Dønstrup, H. Stødkilde-Jørgensen, Low-field NMR relaxation and NMR-imaging as tools in differentiation between potato sample and determination of dry matter content in potatoes, LWT - Food Sci. Technol. 36 (3) (2003) 315–322.
[27] Paola Pittia, Giampiero Sacchetti, Lucia Mancini, Marco Voltolini, Nicola Sodini, Giuliana Tromba, Franco Zanini, Evaluation of microstructural properties of coffee beans by synchrotron X-ray microtomography: a methodological approach, J. Food Sci. 76 (2) (2011) E222–E231.
[28] Y.-Q. Song, Categories of coherence pathways for the CPMG sequence, J. Magn. Reson. 157 (1) (2002) 82–91.
[29] S. Divya, D. Thyagarajan, G. Sujatha, Magnetic resonance imaging technology for process control and quality maintenance in food quality operation, Int. J. Eng. Technol 4 (2013) 441.
[30] B. Zion, S.M. Kim, M.J. McCarthy, P. Chen, Detection of pits in olives under motion by nuclear magnetic resonance, J. Sci. Food Agric. 75 (4) (1997) 496–502.
[31] Asaf Liberman, Elad Bergman, Yifat Sarda, Uri Nevo, Faster imaging with a portable unilateral NMR device, J. Magn. Reson. 231 (2013) 72–78.
[32] Michael Lustig, David L. Donoho, Juan M. Santos, John M. Pauly, Compressed sensing MRI, IEEE Signal Process. Mag. 25 (2) (2008) 72.
[33] Malcolm H. Levitt, Composite pulses, Prog. Nucl. Magn. Reson. Spectrosc. 18 (2) (1986) 61–122.
[34] Martin D. Hürlimann, Encoding of diffusion and T1 in the CPMG echo shape: Single-shot D and T1 measurements in grossly inhomogeneous fields, J. Magn. Reson. 184 (1) (2007) 114–129.